Article

Experimental evidence of neutrinos produced in the CNO fusion cycle in the Sun

https://doi.org/10.1038/s41586-020-2934-0

Received: 26 June 2020

Accepted: 2 October 2020

Published online: 25 November 2020

Check for updates

The Borexino Collaboration*

For most of their existence, stars are fuelled by the fusion of hydrogen into helium. Fusion proceeds via two processes that are well understood theoretically: the proton–proton (*pp*) chain and the carbon–nitrogen–oxygen (CNO) cycle[1,2]. Neutrinos that are emitted along such fusion processes in the solar core are the only direct probe of the deep interior of the Sun. A complete spectroscopic study of neutrinos from the *pp* chain, which produces about 99 per cent of the solar energy, has been performed previously[3]; however, there has been no reported experimental evidence of the CNO cycle. Here we report the direct observation, with a high statistical significance, of neutrinos produced in the CNO cycle in the Sun. This experimental evidence was obtained using the highly radiopure, large-volume, liquid-scintillator detector of Borexino, an experiment located at the underground Laboratori Nazionali del Gran Sasso in Italy. The main experimental challenge was to identify the excess signal—only a few counts per day above the background per 100 tonnes of target—that is attributed to interactions of the CNO neutrinos. Advances in the thermal stabilization of the detector over the last five years enabled us to develop a method to constrain the rate of bismuth-210 contaminating the scintillator. In the CNO cycle, the fusion of hydrogen is catalysed by carbon, nitrogen and oxygen, and so its rate—as well as the flux of emitted CNO neutrinos—depends directly on the abundance of these elements in the solar core. This result therefore paves the way towards a direct measurement of the solar metallicity using CNO neutrinos. Our findings quantify the relative contribution of CNO fusion in the Sun to be of the order of 1 per cent; however, in massive stars, this is the dominant process of energy production. This work provides experimental evidence of the primary mechanism for the stellar conversion of hydrogen into helium in the Universe.

The nuclear fusion mechanisms that are active in stars, the *pp* chain and the CNO cycle, are associated with the production of energy and the emission of a rich spectrum of electron-flavour neutrinos[1,2] (Fig. 1, bottom). The relative importance of these two mechanisms depends mostly on stellar mass and on the abundance of elements in the core that are heavier than helium (the 'metallicity'). For stars that are similar to the Sun but are heavier than about 1.3 solar masses[4] ($M_\odot$), the energy production rate is dominated by the CNO cycle, whereas the *pp* chain prevails in lighter, cooler stars. The CNO cycle is thought to be the primary mechanism for the stellar conversion of hydrogen into helium in the Universe and is estimated to account for 1% of energy production in the Sun; however, the uncertainty is large because the metallicity of the Sun is poorly known. Metallicity is relevant for two reasons: first, 'metals' (namely, carbon, nitrogen and oxygen nuclei) act directly as catalysts in the CNO cycle; and second, they affect the plasma opacity, indirectly changing the temperature of the core and modifying the evolution of the Sun and its density profile. We note that, in the Sun, the CNO sub-cycle I (Fig. 1, top) is dominant[5].

The flux of CNO neutrinos scales with metal abundance in the solar core, which is itself a tracer of the initial chemical composition of the Sun at the time of its formation. The metal abundance in the core is thought to be decoupled from the surface by a radiative zone in which no mixing occurs. CNO neutrinos are therefore a unique probe of the initial condition.

The neutrinos that are produced by the solar *pp* chain have been extensively studied since the early 1970s, leading to the discovery of nuclear fusion reactions in the Sun and of matter-enhanced neutrino flavour conversion[6–14]. Recently, the Borexino experiment has reported a comprehensive study of neutrinos from the *pp* chain[3].

We report here the direct detection of neutrinos from the solar CNO cycle, providing direct evidence of the catalysed hydrogen fusion that was proposed independently by Bethe and Weizsäcker in the 1930s[15,16]. This result quantifies the rate of the CNO cycle in the Sun and paves the way for a solution to the long-standing 'solar metallicity problem'[2]—the discrepancy between the physical properties (for example, the solar sound speed profile and the depth and composition of the external convective envelope) predicted by solar models using updated (low) metal abundances from spectroscopy (low-metallicity standard solar model, SSM-LZ)[17], and those inferred from helioseismology, which favours a higher metal content (high-metallicity standard solar model,

*A list of members and their affiliations appears at the end of the paper.

SSM-HZ). Despite detailed studies, this discrepancy remains an open problem in solar physics.

Our experimental observation of CNO neutrinos confirms the overall solar picture and shows that, with future experimental improvements, a direct measurement of the metallicity of the Sun's core could be within reach.

Borexino detector and data

Borexino is a solar neutrino experiment, located underground at the Laboratori Nazionali del Gran Sasso in Italy, in which the cosmic muon flux is suppressed by a factor of around 10^6. The active core of the detector consists of approximately 280 t of liquid scintillator contained in a spherical nylon vessel with a radius of 4.25 m. Particles that interact in the scintillator emit light, which is detected by 2,212 photomultiplier tubes[18].

Solar neutrinos are detected by Borexino via their elastic scattering off electrons. The total number of detected photons and their arrival times are used to reconstruct the electron recoil energy and the interaction point in the detector, respectively. The energy (E) and spatial resolution (σ) of Borexino has slowly deteriorated over time owing to the steady loss of photomultiplier tubes (on average 1,238 channels are active for this analysis), with current values of $\sigma_E/\sqrt{E} \approx 6\%$ and $\sigma_{x,y,z} \approx 11$ cm for 1 MeV events at the centre of the detector.

The time profile of the scintillation light provides a powerful way to distinguish between different particle types (α, β^- and β^+) via pulse-shape discrimination methods[19,20], and is essential for the selection of ^{210}Po α decays that are used to constrain the ^{210}Bi background, as discussed below.

Despite the very large number of solar neutrinos that reach the Earth, around 6×10^{10} cm^{-2} s^{-1}, their interaction rate is low—namely a few tens of counts per day (cpd) in 100 t of scintillator. Their detection is especially challenging because the signals from neutrinos cannot easily be disentangled from those of radioactive backgrounds. The success of the Borexino experiment is the result of its unprecedented radiopurity combined with the careful selection of materials[21] and clean assembly protocols.

This Article is based on data collected during Phase-III of the Borexino experiment, which ran from July 2016 to February 2020 and corresponds to 1,072 days of live time. The event sample is filtered by applying a set of selection criteria[20] that reduce events from residual radioactive impurities, cosmic muons, cosmogenic isotopes, instrumental noise and external γ-rays. The latter are substantially suppressed by selecting events that occur within an innermost volume of the scintillator (the fiducial volume) as defined by a cut on the reconstructed radius and vertical position ($r < 2.8$ m and -1.8 m $< z < 2.2$ m). The data are analysed in the electron recoil energy interval between 320 keV and 2,640 keV.

The counting rate of events that survive the selection as a function of their visible energy is shown in Fig. 2. The data distribution is understood to be the sum of solar neutrino components and of backgrounds resulting from the decays of residual radioactive contaminants in the scintillator (^{85}Kr, ^{210}Bi, ^{210}Po and ^{40}K) and of cosmogenic ^{11}C, and from γ-rays arising from the decays of ^{40}K, ^{214}Bi and ^{208}Tl in the materials external to the scintillator. These backgrounds were characterized in Phase-II of the Borexino experiment[20] and their counting rates range between a few cpd and tens of cpd per 100 t, compared with the expected CNO signal of a few cpd per 100 t. The key backgrounds for this study are ^{11}C and ^{210}Bi. Together with solar *pep* neutrinos (produced by the proton–electron–proton reaction, an alternative first step of the *pp* chain) they represent the main obstacle in the extraction of the CNO signal, as discussed in the following section. The expected background due to the elastic scattering of ^{40}K geo-antineutrinos[22] is negligible. The yellow vertical band in Fig. 2 highlights the region of largest CNO signal-to-background ratio.

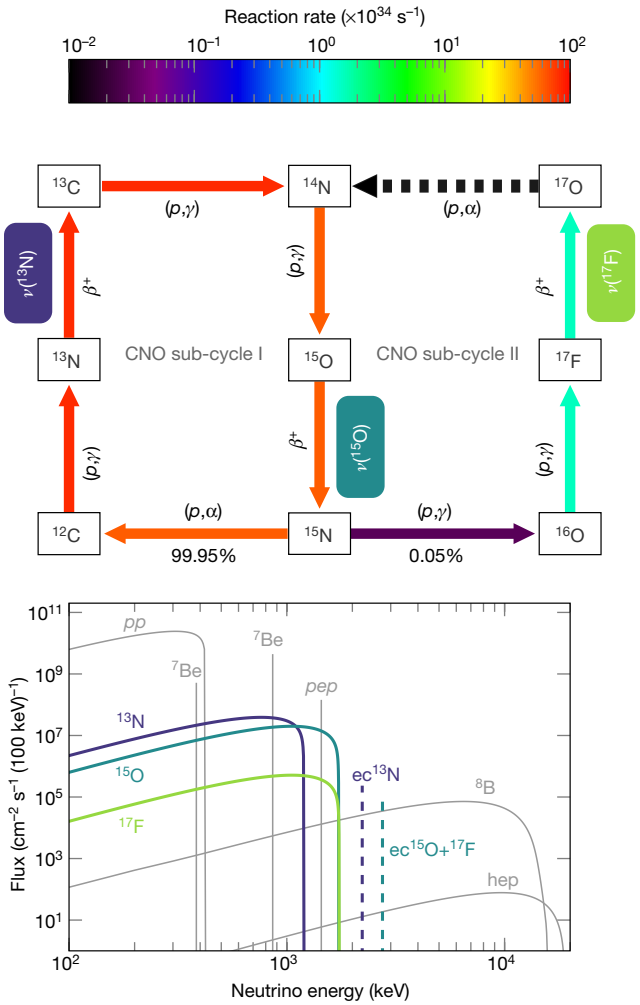

Fig. 1 | CNO nuclear fusion sequences and the energy spectra of solar neutrinos. Top, the double CNO cycle in the Sun, in which sub-cycle I is dominant. The coloured arrows indicate the reaction rates integrated over the volume of the Sun. The rate of the ^{17}O(α, p)^{14}N reaction (dashed arrow) is lower than can be shown on the colour scale. ν, neutrino. Bottom, energy spectra of solar neutrinos from the *pp* chain (grey; representing *pp*, *pep*, ^{7}Be, ^{8}B and ^{3}He–proton (hep) neutrinos and from the CNO cycle (in colour). The two dotted lines indicate electron capture (ec)[39–41]. For mono-energetic lines the flux is given in cm^{-2} s^{-1}.

CNO neutrino detection and the ^{210}Bi challenge

Neutrinos from the CNO cycle have a broad energy spectrum that ranges between 0 and 1,740 keV (see Fig. 1, bottom). Consequently, the recoil energy of electrons has a rather featureless continuous distribution that extends up to 1,517 keV (Fig. 2). In this work, the three CNO neutrino components (Fig. 1) were treated as a single contribution by fixing the ratio between them according to the SSM prediction[1,2]. Several backgrounds contribute to the same energy interval, with a rate comparable to or larger than the signal. To disentangle all contributions, we fit the data with a procedure similar to that adopted in refs. [3,20,23] and described in Methods.

The CNO analysis is affected by two additional complications: the similarity between the spectra of the CNO-neutrino recoil electron and the ^{210}Bi β^- particle, and strong correlations of these spectra with the spectrum of the *pep*-neutrino recoil electron. In addition, in the high-energy region of the CNO spectrum, the data are contaminated by signals from cosmogenic ^{11}C. The muon–neutron–positron threefold-coincidence tagging technique[20] for ^{11}C is essential to enable the detection of CNO neutrinos.

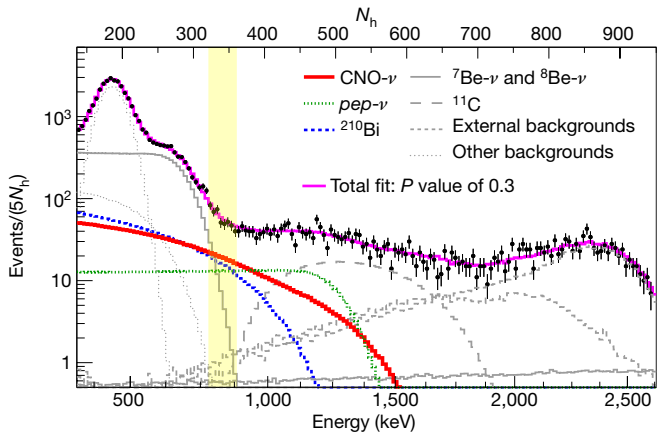

Fig. 2 | Spectral fit of the Borexino data. Distribution of the electron recoil energy scattered by solar neutrinos in the Borexino detector (black points) and corresponding spectral fit (magenta). CNO-neutrinos, ^{210}Bi and *pep*-neutrinos are highlighted in solid red, dashed blue and dotted green, respectively, and all other components are in grey. The energy estimator N_h represents the number of photoelectrons detected by photomultipliers, normalized to 2,000 live channels. The yellow band represents the region with the largest signal-to-background ratio for CNO-neutrinos.

The sensitivity to CNO neutrinos is low unless the ^{210}Bi and *pep*-neutrino rates are sufficiently constrained in the fit[24]. The *pep*-neutrino rate is constrained to 1.4% precision[24], using solar luminosity, robust assumptions on the ratio of *pp*-neutrino rate to *pep*-neutrino rate, existing solar neutrino data[25,26] and the most recent oscillation parameters[27]. We emphasize that the luminosity of the Sun depends very weakly on the contribution of the CNO cycle, making the *pep* constraint essentially independent of any reasonable assumption of the CNO rate.

The other main source of background in the measurement of CNO neutrinos arises from the decays of ^{210}Bi (ref. [24]), a β emitter with a short half-life (5.013 days), the decay rate of which is supported by ^{210}Pb through the sequence:

$$^{210}\mathrm{Pb} \xrightarrow[22.3\,\mathrm{yr}]{\beta^-} {}^{210}\mathrm{Bi} \xrightarrow[5\,\mathrm{d}]{\beta^-} {}^{210}\mathrm{Po} \xrightarrow[138.4\,\mathrm{d}]{\alpha} {}^{206}\mathrm{Pb}. \quad (1)$$

We note that the endpoint energy of the β-decay of ^{210}Pb is 63.5 keV, which is well below the analysis threshold (320 keV). Therefore, in order to determine the ^{210}Bi content we must rely on measuring ^{210}Po (ref. [28]). The α particles from ^{210}Po decay, selected event-by-event by means of pulse-shape discrimination, are ideal tracers of ^{210}Bi, provided that the secular equilibrium in equation (1) is achieved. It is therefore crucial to understand under what conditions such an equilibrium is established.

Since the beginning of the Borexino experiment in 2007, data have indicated the presence of out-of-equilibrium components of ^{210}Po in the scintillator. A dedicated effort was therefore implemented to study these components and, by stabilizing the detector temperature, to ultimately prevent them from migrating into the fiducial volume. This upgrade enabled us to reach a sufficient equilibrium in one central sub-volume of the detector, and therefore to obtain the result that we report here. We distinguish between a scintillator (S) ^{210}Po component (^{210}Po^{S}), which originates from ^{210}Pb in the liquid and is assumed to be stable over time and in equilibrium with ^{210}Bi, and a vessel (V) ^{210}Po component (^{210}Po^{V}). The source of ^{210}Po^{V} for this dataset is understood to be the ^{210}Pb that is deposited on the inner surfaces of the vessel. The daughter ^{210}Po may detach and move into the scintillator by diffusion or by following slow convective currents. It is important to note that, as explained in detail in section '^{210}Bi constraint' below, there is no evidence of ^{210}Pb itself leaching from these surfaces, as the rate of ^{210}Bi observed in the scintillator has shown negligible change over several years.

The diffusion length of ^{210}Po atoms in one half-life is considerably less than the separation between the vessel and the fiducial volume (approximately 1 m). We can therefore conclude that diffusion is negligible for both ^{210}Po and ^{210}Bi. However, data from the Borexino experiment show that slow convective currents—caused by temperature gradients and temperature variations—might in fact carry ^{210}Po into the fiducial volume. This does not occur for the short-lived ^{210}Bi, which might also detach from the vessel, because it decays before reaching the fiducial volume.

Before 2016, Borexino was not equipped with detailed temperature mapping, thermal insulation or active temperature control. Convective currents were substantial, because of seasonal temperature variations and human activities affecting the temperature of the experimental hall. The large fluctuations in the activity of ^{210}Po in the fiducial volume that were induced by these currents are shown in Fig. 3, in which the ^{210}Po rate at different detector positions is plotted as a function of time. It is evident that, before 2016, the ^{210}Po counts in the fiducial volume were both high (>100 cpd per 100 t) and very unstable on timescales shorter than the ^{210}Po half-life, because of sizeable fluid movements that prevented the separation of the scintillator Po component from the vessel Po component.

In order to suppress convection, it was necessary to establish a stable vertical thermal gradient. The Borexino installation sits atop a cold floor in contact with rock that can act as an infinite thermal sink, thereby providing an opportunity to achieve such a gradient if the detector is insulated against instabilities in air temperature. Thermal insulation of the detector was completed in December 2015, and in January 2016 an active temperature control system[29] was installed on top of the detector (see Methods). A residual seasonal modulation of the order of 0.3 °C over 6 months is still visible in the detector and in the rock below it, but its effect is small for the purpose of the results reported here.

After this extensive stabilization effort, the ^{210}Po rate initially decreased and reached its lowest value in a region that we named the low polonium field (LPoF), above the equator at $z \approx +80$ cm. The existence of this volume, which is compatible in terms of size and location with fluid dynamics simulation[30], is crucial in determining the ^{210}Bi constraint. We note that the result we report here is stable to small variations in the shape and the location of the low polonium field.

^{210}Bi constraint

The amount of ^{210}Bi in the scintillator is determined from the minimum value of the ^{210}Po rate $R(^{210}\mathrm{Po}_{\mathrm{min}})$ in the low polonium field through the relation:

$$R(^{210}\mathrm{Po}_{\mathrm{min}}) = R(^{210}\mathrm{Bi}) + R(^{210}\mathrm{Po}^{V}), \quad (2)$$

where the ^{210}Bi rate is equal to ^{210}Po^{S} according to secular equilibrium. Because ^{210}Po^{V} is always positive, ^{210}Po$_{\mathrm{min}}$ yields an upper limit for the ^{210}Bi rate.

The ^{210}Po content is not spatially uniform within the low polonium field but exhibits a clear minimum with no sizable plateau around it. This yields a robust upper limit for the rate of ^{210}Bi, but does not guarantee that ^{210}Po^{V} is actually zero. Only a spatially extended minimum of the ^{210}Po rate would have yielded a measurement of the ^{210}Bi rate.

The minimum ^{210}Po rate was estimated from the ^{210}Po distribution within the low polonium field using 2D and 3D fits following two mutually compatible procedures (see Methods). The spatial position of the minimum is stable over the analysis period—it moves slowly by less than 20 cm per month—which shows that the detector is in a fluid-dynamical quasi-steady-state condition and that the ^{210}Po rate minimum is not a statistical fluctuation. Both procedures consistently yield $R(^{210}\mathrm{Po}_{\mathrm{min}}) = 11.5 \pm 1.0$ cpd per 100 t. The error includes the systematic uncertainty of the fit (see Methods).

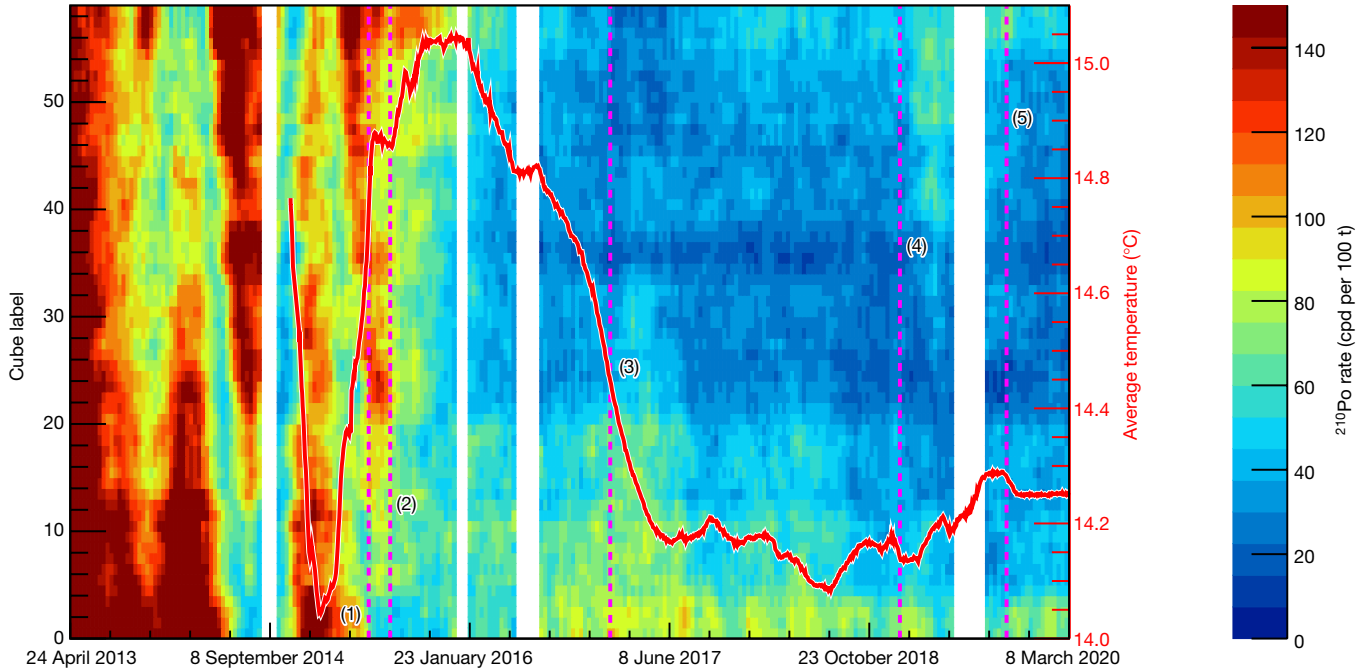

Fig. 3 | Spatial and temporal distribution of ^{210}Po activity. ^{210}Po rate in Borexino in cpd per 100 t (rainbow colour scale) as a function of time. Small cubes of about 3 t each are ordered from the bottom (0) to the top (58) along the vertical direction (latest update: March 2020). All cubes are selected inside a sphere of radius $r = 3$ m. The red curve represents the average temperature in the innermost region surrounding the nylon vessel. The dashed vertical lines indicate the most important milestones of the temperature stabilization program: (1) beginning of the 'insulation program'; (2) turning off of the water recirculation system in the water tank; (3) first operation of the active temperature control system; (4) change of the active control set point; (5) installation and commissioning of the hall temperature control system. The white vertical bands represent different interruptions to the data acquisition due to technical issues.

The ^{210}Bi rate can then be extrapolated over the whole fiducial volume, provided that it is uniform in the fiducial volume during the time period over which the estimation is performed. Because it is not possible to individually tag ^{210}Bi events, the analysis is performed by selecting β-like events at energies at which the relative bismuth contribution is maximal. We find that the angular and spatial distribution of ^{210}Bi is uniform within errors. The systematic uncertainty associated with possible spatial non-uniformity of ^{210}Bi is conservatively estimated at 0.78 cpd per 100 t. The observed ^{210}Bi uniformity in Phase-III of the Borexino experiment is expected as a result of the substantial fluid mixing that occurred before the thermal insulation, and agrees with 2D and 3D fluid dynamic simulations.

Because of the low velocity of convection currents, the uniformity of ^{210}Bi provides convincing evidence that ^{210}Pb does not leach off the vessel. As a cross-check, the rate of β-like events shows the expected annual modulation of the solar neutrino rate of 3.3%—dominated by ^{7}Be-neutrinos—as a result of the eccentricity of the Earth's orbit, thus proving that background β-like events are stable in time. Further details are provided in Methods.

In summary, the ^{210}Bi rate used as a constraint in the CNO-neutrino analysis is

$$R(^{210}\mathrm{Bi}) \leq 11.5 \pm 1.3 \text{ cpd per } 100 \text{ t}, \quad (3)$$

which includes the statistical and systematic uncertainties in the determination of the ^{210}Po minimum, and the systematic uncertainty related to the ^{210}Bi uniformity hypothesis (added in quadrature).

Results and conclusions

We performed a multivariate analysis, simultaneously fitting the energy spectra in the window between 320 keV and 2,640 keV and the radial distribution of the selected events (see Methods for details). The following rates were treated as free parameters: CNO-neutrinos, ^{85}Kr, ^{11}C, internal and external ^{40}K, external ^{208}Tl and ^{214}Bi and ^{7}Be-neutrinos. The *pep*-neutrino rate is constrained to 2.74 ± 0.04 cpd per 100 t by multiplying the standard likelihood by a symmetric Gaussian term. The upper limit to the ^{210}Bi rate obtained from equation (3) is enforced asymmetrically by multiplying the likelihood by a half-Gaussian term—that is, leaving the ^{210}Bi rate unconstrained between 0 and 11.5 cpd per 100 t.

The reference spectral and radial probability density functions of each signal and background species that are used in the multivariate fit are obtained with a complete Monte Carlo simulation based on Geant4[20,31]. The results of the multivariate fit for data in which the ^{11}C contribution has been subtracted with the threefold-coincidence technique are shown in Fig. 2. The P value of the fit is high (0.3), which demonstrates good agreement between the data and the underlying fit model. The corresponding negative log-likelihood for CNO-neutrinos, profiled over the other neutrino fluxes and background sources, is shown in Fig. 4. The best fit value is 7.2 cpd per 100 t, with an asymmetric confidence interval of −1.7 cpd per 100 t and +2.9 cpd per 100 t (68% confidence level, statistical error only), obtained from the quantile of the likelihood profile.

We studied possible sources of systematic error following an approach similar to that used in refs. [3,20]. By performing 2,500 fits with different fit ranges and binning values, we found that the effect of varying these fit parameters was negligible with respect to the CNO statistical uncertainty. We also considered the effect of different theoretical ^{210}Bi shapes from refs. [32–34] and found that the CNO result is robust with respect to the selected shape[32]. Differences in CNO rate are included in the systematic error. We performed a detailed study of the effect of possible deviations of the energy scale and resolution from the Monte Carlo model: nonlinearity, non-uniformity and variation in the absolute magnitude of the scintillator light yield were investigated by simulating several million Monte Carlo pseudo-experiments with deformed shapes and fitting them with the regular non-deformed

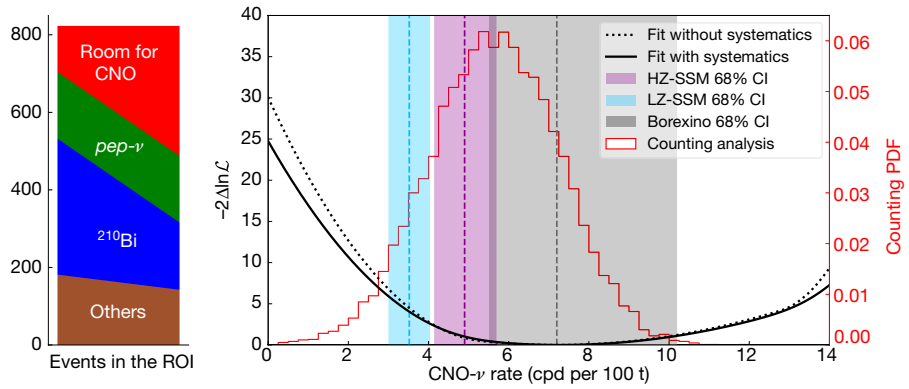

Fig. 4 | Results of the CNO counting and spectral analyses. Left, counting analysis bar chart. The height represents the number of events allowed by the data for CNO-neutrinos and backgrounds in the region of interest (ROI). On the left, the CNO signal is minimum and backgrounds are maximum; on the right, CNO is maximum and backgrounds are minimum. It is clear from this figure that the contribution of CNO neutrinos cannot be zero. Right, CNO-neutrino rate negative log-likelihood ($\ln\mathcal{L}$) profile obtained directly from the multivariate fit (dashed black line) and after folding in the systematic uncertainties (black solid line). The histogram in red shows the CNO-neutrino rate obtained from the counting analysis. The blue, violet and grey vertical bands show 68% confidence intervals (CI) for the SSM-LZ (3.52 ± 0.52 cpd per 100 t) and SSM-HZ (4.92 ± 0.78 cpd per 100 t)[2,24] predictions and the Borexino result (corresponding to the black solid-line log-likelihood profile), respectively.

probability density functions. The magnitude of the deformations was chosen to be within the range allowed by the available calibrations[35] and by two 'standard candles' (^{210}Po, ^{11}C) present in the data. The overall contribution to the total error of all these sources is $^{+0.6}_{-0.5}$ cpd per 100 t. Folding the systematic uncertainty over the log-likelihood profile we determine the final CNO interaction rate to be $7.2^{+3.0}_{-1.7}$ cpd per 100 t. This rate can be converted to a flux of CNO-neutrinos on Earth of $7.0^{+3.0}_{-2.0} \times 10^8$ cm^{-2} s^{-1}, assuming Mikheyev–Smirnov–Wolfenstein conversion in matter[36], neutrino oscillation parameters from ref. [37] and references therein, and a density of electrons in the scintillator of $(3.307 \pm 0.015) \times 10^{31}\,e^-$ per 100 t.

Other sources of systematic error that were investigated in the previous precision measurement of the *pp* chain[3]—such as fiducial volume, scintillator density and lifetime—were found to be negligible with respect to the large CNO statistical uncertainty.

The log-likelihood profile including all the errors combined in quadrature is shown in Fig. 4. The asymmetry of the profile is a result of applying a half-Gaussian constraint on the ^{210}Bi (see equation (3)) and causes the profile to be relatively steep on the left-hand side of the minimum. The shallow curve on the right-hand side of the profile reflects the modest sensitivity in distinguishing the spectral shapes of the ^{210}Bi and the CNO recoil spectra. From the corresponding profile-likelihood we obtain a significance of 5.1σ for the CNO observation. Additionally, a hypothesis test based on a profile likelihood test statistics[38]—using 13.8 million pseudo-datasets with the same exposure as the Phase-III experiment and including systematic uncertainties (see Methods)—excludes the no-CNO signal scenario with a significance greater than 5.0σ at a 99.0% confidence level.

The observed CNO rate is compatible with both SSM-HZ and SSM-LZ predictions, and as such we cannot distinguish between the two different models: the statistical compatibility for HZ is 0.5σ and for LZ is 1.3σ (Fig. 4). When combined with other solar neutrino fluxes measured by the Borexino experiment, the LZ hypothesis is disfavoured at a level of 2.1σ.

We emphasize that the sensitivity to CNO neutrinos arises mainly from a small energy region between 780 keV and 885 keV (the region of interest; see yellow band in Fig. 2) at which the signal-to-background ratio is maximal[24]. In this region, the count rate is dominated by events from CNO and *pep* neutrinos, and by ^{210}Bi decays. The remaining backgrounds contribute less than 20% (Fig. 4). A simple counting analysis confirms that the number of events in the region of interest exceeds the sum from all known backgrounds, leaving room for CNO neutrinos (Fig. 4). In this simplified approach (described in detail in Methods), we use the ^{210}Bi rate (as in equation (3)) and apply a symmetric Gaussian penalty while assuming an analytical description of the background model and the detector response. After accounting for statistical and systematic errors, the statistical significance of the presence in the data of CNO neutrino events from this counting analysis is around 3.5σ, which is lower than that obtained with the main analysis given the simplified nature of this approach. In conclusion, the absence of a CNO solar neutrino signal is excluded with a significance of 5.0σ. We therefore present a direct detection of CNO solar neutrinos.

Online content

Any methods, additional references, Nature Research reporting summaries, source data, extended data, supplementary information, acknowledgements, peer review information; details of author contributions and competing interests; and statements of data and code availability are available at https://doi.org/10.1038/s41586-020-2934-0.

1. Bahcall, J. N. *Neutrino Astrophysics* (Cambridge Univ. Press, 1989).
2. Vinyoles, N. et al. A new generation of standard solar models. *Astrophys. J.* **835**, 202 (2017).
3. The Borexino Collaboration. Comprehensive measurement of *pp*-chain solar neutrinos. *Nature* **562**, 505–510 (2018).
4. Salaris, M. & Cassisi, S. *Evolution of Stars and Stellar Populations* (John Wiley & Sons, 2005).
5. Angulo, C. et al. A compilation of charged-particle induced thermonuclear reaction rates. *Nucl. Phys. A* **656**, 3–183 (1999).
6. Davis, R. Jr *A Half-Century with Solar Neutrinos*. Nobel Prize Lecture https://www.nobelprize.org/prizes/physics/2002/davis/lecture/ (2002).
7. GALLEX collaboration. Solar neutrinos observed by GALLEX at Gran Sasso. *Phys. Lett. B* **285**, 376 (1992).
8. SAGE collaboration. Results from SAGE (The Russian–American Gallium solar neutrino experiment). *Phys. Lett. B* **328**, 234 (1994).
9. McDonald, A. B. *The Sudbury Neutrino Observatory: Observation of Flavor Change for Solar Neutrinos*. Nobel Prize Lecture https://www.nobelprize.org/prizes/physics/2015/mcdonald/lecture/ (2015).
10. Hirata, K. et al. Observation of ^{8}B solar neutrinos in the Kamiokande-II detector. *Phys. Rev. Lett.* **63**, 16 (1989).
11. Ahmad, Q. et al. Direct evidence for neutrino flavor transformation from neutral-current interactions in the Sudbury Neutrino Observatory. *Phys. Rev. Lett.* **89**, 011301 (2002).
12. Araki, T. et al. Measurement of neutrino oscillation with KamLAND: evidence of spectral distortion. *Phys. Rev. Lett.* **94**, 081801 (2005).
13. Borexino Collaboration. Neutrinos from the primary proton–proton fusion process in the Sun. *Nature* **512**, 383–386 (2014).
14. Bellini, G. et al. Precision measurement of the ^{7}Be solar neutrino interaction rate in Borexino. *Phys. Rev. Lett.* **107**, 141302 (2011).
15. Bethe, H. A. Energy production in stars. *Phys. Rev.* **55**, 434–456 (1939).
16. von Weizsäcker, C. F. Über Elementumwandlungen im Innern der Sterne I. *Phys. Z.* **38**, 176 (1937).
17. Serenelli, A. M., Haxton, W. C. & Peña-Garay, C. Solar models with accretion. I. application to the solar abundance problem. *Astrophys. J.* **743**, 24 (2011).

18. Alimonti, G. et al. The Borexino detector at the Laboratori Nazionali del Gran Sasso. *Nucl. Instrum. Methods Phys. Res. A* **600**, 568–593 (2009).
19. Bellini, G. et al. Final results of Borexino Phase-I on low-energy solar neutrino spectroscopy. *Phys. Rev. D* **89**, 112007 (2014).
20. Agostini, M. et al. Simultaneous precision spectroscopy of *pp*, ^{7}Be and *pep* solar neutrinos with Borexino Phase-II. *Phys. Rev. D* **100**, 082004 (2019).
21. Alimonti, G. et al. Science and technology of BOREXINO: a real-time detector for low energy solar neutrinos. *Astropart. Phys.* **16**, 205–234 (2002).
22. Agostini, M. et al. Comprehensive geoneutrino analysis with Borexino. *Phys. Rev. D* **101**, 012009 (2020).
23. Ding, X. F. GooStats: A GPU-based framework for multi-variate analysis in particle physics. *J. Instrum.* **13**, P12018 (2018).
24. Agostini, M. et al. Sensitivity to neutrinos from the solar CNO cycle in Borexino. *Eur. Phys. J. C* https://doi.org/10.1140/epjc/s10052-020-08534-2 (2020).
25. Vissani, F. Luminosity constraint and entangled solar neutrino signals. In *Solar Neutrinos, Proc. 5th International Solar Neutrino Conference* (eds Meyer, M. & Zuber, K.) 121–141 (World Scientific, 2019).
26. Bergström, J., Gonzalez-Garcia, M. C., Maltoni, M., Peña-Garay, C., Serenelli, A. M. & Song, N. Updated determination of the solar neutrino fluxes from solar neutrino data. *J. High Energy Phys.* **2016**, 132 (2016).
27. Capozzi, F., Lisi, E., Marrone, A. & Palazzo, A. Global analysis of oscillation parameters. *J. Phys. Conf. Ser.* **1312**, 012005 (2019).
28. Villante, F. L., Ianni, A., Lombardi, F., Pagliaroli, G. & Vissani, F. A step toward CNO solar neutrino detection in liquid scintillators. *Phys. Lett. B* **701**, 336–341 (2011).
29. Bravo-Berguño, D. et al. The Borexino Thermal Monitoring & Management System and simulations of the fluid-dynamics of the Borexino detector under asymmetrical, changing boundary conditions. *Nucl. Instrum. Methods Phys. Res. A* **885**, 38–53 (2018).
30. Di Marcello, V. et al. Fluid-dynamics and transport of ^{210}Po in the scintillator Borexino detector: a numerical analysis. *Nucl. Instrum. Methods Phys. Res. A* **964**, 163801 (2020).
31. Agostini, M. et al. The Monte Carlo simulation of the Borexino detector. *Astropart. Phys.* **97**, 136–159 (2018).
32. Daniel, H. Das β-spektrum des RaE. *Nucl. Phys.* **31**, 293–307 (1962).
33. Grau Carles, A. & Grau Malonda, A. Precision measurement of the RaE shape factor. *Nucl. Phys. A* **596**, 83–90 (1996).
34. Alekseev, I. E. et al. Precision measurement of ^{210}Bi β-spectrum. Preprint at https://arxiv.org/abs/2005.08481 (2020).
35. Back, H. et al. Borexino calibrations: hardware, methods, and results. *J. Instrum.* **7**, P10018 (2012).
36. de Holanda, P. C., Liao, W. & Smirnov, A. Yu. Toward precision measurements in solar neutrinos. *Nucl. Phys. B* **702**, 307–332 (2004).
37. Capozzi, F., Lisi, E., Marrone, A. & Palazzo, A. Current unknowns in the three neutrino framework. *Prog. Part. Nucl. Phys.* **102**, 48–72 (2018).
38. Cowan, G., Cranmer, K., Gross, E. & Vitells, O. Asymptotic formulae for likelihood-based tests of new physics. *Eur. Phys. J. C* **71**, 1554 (2011).
39. Bahcall, J. N. Line versus continuum solar neutrinos. *Phys. Rev. D* **41**, 2964–2966 (1990).
40. Stonehill, L. C., Formaggio, J. A. & Robertson, R. G. H. Solar neutrinos from CNO electron capture. *Phys. Rev. C* **69**, 015801 (2004).
41. Villante, F. L. ecCNO solar neutrinos: a challenge for gigantic ultra-pure liquid scintillator detectors. *Phys. Lett. B* **742**, 279–284 (2015).

Publisher's note Springer Nature remains neutral with regard to jurisdictional claims in published maps and institutional affiliations.

© The Author(s), under exclusive licence to Springer Nature Limited 2020

The Borexino Collaboration

M. Agostini[1,2], K. Altenmüller[2], S. Appel[2], V. Atroshchenko[3], Z. Bagdasarian[4,27], D. Basilico[5], G. Bellini[5], J. Benziger[6], R. Biondi[7], D. Bravo[5,28], B. Caccianiga[5], F. Calaprice[8], A. Caminata[9], P. Cavalcante[10,29], A. Chepurnov[11], D. D'Angelo[5], S. Davini[9], A. Derbin[12], A. Di Giacinto[7], V. Di Marcello[7], X. F. Ding[8], A. Di Ludovico[8], L. Di Noto[9], I. Drachnev[12], A. Formozov[5,13], D. Franco[14], C. Galbiati[8,15], C. Ghiano[7], M. Giammarchi[5], A. Goretti[8,29], A. S. Göttel[4,16], M. Gromov[11,13], D. Guffanti[17], Aldo Ianni[7], Andrea Ianni[8], A. Jany[18], D. Jeschke[2], V. Kobychev[19], G. Korga[20,21], S. Kumaran[4,16], M. Laubenstein[7], E. Litvinovich[3,22], P. Lombardi[5], I. Lomskaya[12], L. Ludhova[4,16], G. Lukyanchenko[3], L. Lukyanchenko[3], I. Machulin[3,22], J. Martyn[17], E. Meroni[5], M. Meyer[23], L. Miramonti[5], M. Misiaszek[18], V. Muratova[12], B. Neumair[2], M. Nieslony[17], R. Nugmanov[3,22], L. Oberauer[2], V. Orekhov[17], F. Ortica[24], M. Pallavicini[9], L. Papp[2], L. Pelicci[5], Ö. Penek[4,16], L. Pietrofaccia[8], N. Pilipenko[12], A. Pocar[25], G. Raikov[3], M. T. Ranalli[7], G. Ranucci[5] ✉, A. Razeto[7], A. Re[5], M. Redchuk[4,16], A. Romani[24], N. Rossi[7], S. Schönert[2], D. Semenov[12], G. Settanta[4], M. Skorokhvatov[3,22], A. Singhal[4,16], O. Smirnov[13], A. Sotnikov[13], Y. Suvorov[3,7,30], R. Tartaglia[7], G. Testera[9], J. Thurn[23], E. Unzhakov[12], F. L. Villante[7,26], A. Vishneva[13], R. B. Vogelaar[10], F. von Feilitzsch[2], M. Wojcik[18], M. Wurm[17], S. Zavatarelli[9], K. Zuber[23] & G. Zuzel[18]

[1]Department of Physics and Astronomy, University College London, London, UK. [2]Physik-Department E15, Technische Universität München, Garching, Germany. [3]National Research Centre Kurchatov Institute, Moscow, Russia. [4]Institut für Kernphysik, Forschungszentrum Jülich, Jülich, Germany. [5]Dipartimento di Fisica, Università degli Studi and INFN, Milan, Italy. [6]Chemical Engineering Department, Princeton University, Princeton, NJ, USA. [7]INFN Laboratori Nazionali del Gran Sasso, Assergi, Italy. [8]Physics Department, Princeton University, Princeton, NJ, USA. [9]Dipartimento di Fisica, Università degli Studi and INFN, Genoa, Italy. [10]Physics Department, Virginia Polytechnic Institute and State University, Blacksburg, VA, USA. [11]Lomonosov Moscow State University Skobeltsyn Institute of Nuclear Physics, Moscow, Russia. [12]St Petersburg Nuclear Physics Institute, NRC Kurchatov Institute, Gatchina, Russia. [13]Joint Institute for Nuclear Research, Dubna, Russia. [14]Astroparticule et Cosmologie, Université de Paris, CNRS, Paris, France. [15]Gran Sasso Science Institute, L'Aquila, Italy. [16]III. Physikalisches Institut B, RWTH Aachen University, Aachen, Germany. [17]Institute of Physics and Excellence Cluster PRISMA+, Johannes Gutenberg-Universität Mainz, Mainz, Germany. [18]M. Smoluchowski Institute of Physics, Jagiellonian University, Krakow, Poland. [19]Institute for Nuclear Research of NAS Ukraine, Kyiv, Ukraine. [20]Department of Physics, School of Engineering, Physical and Mathematical Sciences, Royal Holloway, University of London, Egham, UK. [21]Institute of Nuclear Research (Atomki), Debrecen, Hungary. [22]National Research Nuclear University MEPhI (Moscow Engineering Physics Institute), Moscow, Russia. [23]Department of Physics, Technische Universität Dresden, Dresden, Germany. [24]Dipartimento di Chimica, Biologia e Biotecnologie, Università degli Studi e INFN, Perugia, Italy. [25]Amherst Center for Fundamental Interactions and Physics Department, University of Massachusetts, Amherst, MA, USA. [26]Dipartimento di Scienze Fisiche e Chimiche, Università dell'Aquila, L'Aquila, Italy. [27]Present address: Department of Physics, University of California, Berkeley, Berkeley, CA, USA. [28]Present address: Departamento de Física Teórica, Universidad Autónoma de Madrid, Madrid, Spain. [29]Present address: INFN Laboratori Nazionali del Gran Sasso, Assergi, Italy. [30]Present address: Dipartimento di Fisica, Università degli Studi Federico II e INFN, Naples, Italy. ✉e-mail: spokesperson-borex@lngs.infn.it

Methods

Experimental setup and neutrino detection technique

The Borexino detector[18] was designed and built to achieve the utmost radiopurity at its core. It is made of an unsegmented stainless steel sphere (SSS) mounted within a large water tank. The SSS contains the organic liquid and supports the photomultiplier tubes (PMTs), while the water shields the SSS against external radiation and is the active medium of a Cherenkov muon tagger. A schematic is shown in Extended Data Fig. 1.

Within this SSS, two thin (125 μm) nylon vessels separate the volume in three shells of radii 4.25 m, 5.50 m and 6.85 m, the latter being the radius of the SSS itself.

The inner nylon vessel, concentric to the SSS, contains a solution of pseudocumene as solvent and 2,5-diphenyloxazole (PPO) as fluor dissolved at a concentration of about 1.5 g l^{-1}. The second and the third shells are filled with a buffer liquid comprised of a solution of dimethylphthalate (DMP) in pseudocumene. The purpose of this double buffer is to shield the inner vessel against γ radiation emitted by contaminants present in the PMTs and the steel, while the outer nylon vessel prevents the diffusion of emanated radon into the inner vessel. The total amount of liquid within the SSS is approximately 1,300 t, of which about 280 t are the active liquid scintillator.

The inner vessel scintillator density is slightly smaller than that of the buffer liquid, yielding an upward buoyant force. The inner vessel is therefore anchored to the bottom of the SSS through thin high-molecular-weight polyethylene cords, thus minimising the amount of material close to the scintillator and keeping the inner vessel in stable mechanical equilibrium.

The SSS is equipped with nominally 2,212 8-inch (20.3 cm) PMTs that collect scintillation light emitted when a charged particle, either produced by neutrino interactions or by radioactivity, releases energy in the scintillator. Most of the PMTs (1,800) are equipped with light concentrators (Winston cones) for an effective optical coverage of 30%. Scintillation light is detected at approximately 500 photoelectrons per MeV of electron equivalent of deposited energy (normalized to 2,000 PMTs). In organic liquid scintillators, the light yield per unit of deposited energy is affected by ionization quenching[42]. Alpha particles, characterized by higher ionization rates along their path, experience more quenching compared to electrons and thus produce less scintillation light. The distribution of photon arrival times on PMTs allows the reconstruction of the location of the energy deposit by means of time-of-flight triangulation and the determination of the particle type by exploiting the pulse shape[20].

The very nature of the scintillation emission makes it impossible to distinguish the signal emitted by electrons scattered by neutrinos from that produced by electrons emitted in nuclear β-decays or Compton-scattered by γ-rays. Therefore, the radioactive background must be kept at or below the level of the expected signal rate, which for the total solar neutrino spectrum is of the order of a few events per tonne per day and, in the case of CNO neutrinos, two orders of magnitude smaller. Taking into account that typical materials (air, water, metals) are normally contaminated with radioactive impurities at the level of 10,000 or even 100,000 decays per tonne per second, this requirement is indeed a formidable challenge.

The scintillator procurement procedure was conceived to select an organic hydrocarbon with a very low ^{14}C (β^-, with the total energy released (the Q-value) being $Q = 156$ keV) content. Carbon-14 is cosmogenically activated in atmospheric carbon and an irreducible radioactive contaminant in organic hydrocarbons. The scintillator was delivered to the Gran Sasso laboratory in special tanks following procedures conceived to avoid contamination and to minimize the exposure to cosmic rays, which also produce other long-living isotopes. Once underground, it was purified following various steps in plants specifically developed over more than 10 years for this purpose and installed close to the detector. The purification during the initial scintillator fill in 2007 was done mainly by distillation and counterflow sparging using low-argon-krypton nitrogen. A dedicated purification campaign in 2010–2011 processed the scintillator through several cycles of ultra-pure water extraction. These purification techniques are described in refs. [20,43,44].

After this effort, the extreme purity of the scintillator and the careful selection of the material surrounding it (nylon, plastic supports of the nylon vessels, steel and PMT glass in particular), and the use of carefully selected components (valves, pumps, fittings, etc.) together with special care during detector construction and installation, yielded unprecedented low values of radioactive contaminants in the active scintillator. In addition, through the selection of a fiducial volume, the residual external gamma ray background (from the interval vessel nylon, the SSS and the PMTs) is further substantially reduced. All results from the Borexino experiment can be directly attributed to this unprecedented radiopurity.

The water tank is itself equipped with 208 PMTs to detect Cherenkov light emitted by muons crossing the water. The capability to detect muons and to reconstruct their tracks through the scintillator was crucial to identify and tag cosmogenic contaminants (that is, short-lived nuclei produced by muon spallation with scintillator components[45,46]), especially the ^{11}C background. Muon tagging enables Borexino to also efficiently detect cosmogenic neutrons[47], which occasionally are produced with high multiplicity, another crucial ingredient in ^{11}C tagging.

Thermal insulation system and control

The thermal stability of the Borexino detector is required to avoid undesired background variations due to the mixing of the scintillator inside the inner vessel. This mixing is caused by convective currents induced by temperature changes due to human activities in the underground hall and to seasonal effects. A substantial upgrade of the detector in this respect was carried out.

Between May and December 2015, 900 m^2 of thermal insulation was installed on the outside of the Borexino water tank. In addition, the system used to recirculate water inside the water tank was stopped in July 2015 to contribute to the inner detector thermal stability and allow its fluid to vertically stratify.

The thermal insulation consists of two layers: an outer 10-cm layer of Ultimate Tech Roll 2.0 mineral wool (thermal conductivity at 10 °C of 0.033 W m^{-1} K^{-1}) and an inner 10-cm layer of Ultimate Protect wired Mat 4.0 mineral wool reinforced with Al foil (65 g cm^{-2}) with glass grid on one side (thermal conductivity at 10 °C of 0.030 W m^{-1} K^{-1}). The thermal insulation material is anchored to the water tank with 20-m-long nails on a metal plate attached to the tank (5 nails per m^2). In addition, an active temperature control system (ATCS) was completed in January 2016. Extended Data Fig. 2 shows the Borexino water tank wrapped in thermal insulation.

A system of 66 probes with 0.07 °C resolution, the position of which is shown in Extended Data Fig. 3, monitors the temperature of Borexino. They are arranged as follows: 14 protruding 0.5 m radially inward into the SSS (ReB probes), in operation since October 2014, measure the temperature of the outer part of the buffer liquid; 14 mounted 0.5 m radially outward from the SSS (ReW probes), in operation since April 2015, measure the temperature of the water; 20 installed between the insulation layer and the external surface of the water tank (WT probes), in operation since May 2015; 4 located inside a pit underneath the Borexino water tank, in operation since October 2015; 14 on the Borexino detector water tank dome, installed in early 2016. Since 2016 the average temperature of the floor underneath the detector in contact with the rock is 7.5 °C, whereas at the top of the detector it is 15.8 °C. This temperature difference corresponds to a naturally driven gradient $\Delta T/\Delta z > 0 \approx 0.5$ °C m^{-1}. Ensuring this gradient does not decrease is the key to reducing convective currents and scintillator mixing, and consequently to stabilizing the ^{210}Po background for the CNO analysis.

Out of the last 14 probes, three are part of the ATCS. The ATCS consists of a water-based system made with copper tube coils installed on the upper part of the dome of the detector. The coils are in contact with the water tank steel, with the addition of an Al layer to enhance the thermal coupling. A 3-kW electric heater, a circulation pump, a temperature controller and an expansion tank are connected to the coils. The ATCS trims the natural thermal gradient and is essential to eliminate convection motion.

The outer detector head tank (a 70-l vessel connected with the 1,346 m^3 volume of the SSS) is used as a sensitive detector thermometer. After installation of the thermal insulation system the head tank had to be refilled with 289 kg of pseudocumene because of the overall cooling of the detector and corresponding shrinkage. Calibration established the sensitivity of this thermometer to be of the order of 10^{-2} °C per 100 mm change of fluid height.

The deployment of both the thermal insulation and the temperature control systems were quickly effective in stabilizing the inner detector temperature. As of 2016 the heat loss due to the thermal insulation system was equal to 247 W. However, changes of the experimental hall temperature induced residual variations in the top buffer probes of the order of 0.3 °C over 6 months. To further reduce these effects, an active system to control the seasonal changes in the air temperature entering the experimental hall and surrounding the Borexino water tank was designed and installed in 2019. It consists of a 70-kW electrical heater installed inside the inlet air duct, which has a capacity of 12,000 $m^3\,h^{-1}$ (in normal conditions). The heater is deployed just a few metres before the main door to the hall. The temperature control is based on a master/slave architecture with a master PID (proportional–integral–derivative) controller that acts on a second slave PID controller. Probes deployed around the water tank monitor the temperature of the air. After commissioning, a set point temperature for the master PID of 14.5 °C is chosen. This system controls the temperature of the inlet air within approximately 0.05 °C.

The thermal insulation, active temperature control of the detector, and control of the air temperature in the hall have enabled remarkable temperature stability of the detector. Extended Data Fig. 4 shows the temperature time profile read by all probes since 2016. A stable temperature gradient was clearly established, as required to avoid mixing of the scintillator.

The low polonium field and its properties

After the completion of the thermal insulation (Phase-III), the ^{210}Bi background activity is measured from the ^{210}Po activity assuming secular equilibrium of the mass number $A = 210$ chain. The measured ^{210}Po rate is the sum of two contributions: a scintillator ^{210}Po component supported by the ^{210}Pb in the liquid ($^{210}Po^{S}$), which we assume to be stable in time and equal to the intrinsic rate of ^{210}Bi in the scintillator, and a vessel component ($^{210}Po^{V}$). The latter has a 3D diffusive-like structure as a result of polonium detaching from the inner vessel and migrating into the fiducial volume. The origin of this component is the ^{210}Pb contamination of the vessel. The ^{210}Po migration process is driven by residual convective currents. A rough estimation of the migration length λ_{mig}, obtained by fitting the spatial distribution of ^{210}Po, is found to range between 50 and 100 cm, which corresponds to a migration coefficient $D_{mig} = (1.0 \pm 0.4) \times 10^{-9}\ m^2\,s^{-1}$ (where we have used the relation $\lambda_{mig} = \sqrt{D_{mig}\tau_{Po}}$ with the ^{210}Po lifetime, $\tau_{Po} = 199.7$ days). This value is slightly lower than the diffusion coefficient $D_{diff} \approx 1.5 \times 10^{-9}\ m^2\,s^{-1}$ (corresponding to a diffusion length $\lambda_{diff} \approx 20$ cm), predicted by the Stokes–Einstein formula[48] and observed for heavy atoms in hydrocarbons[49]. We attribute this difference to the presence of residual convective motions in Phase-III. These motions are localized in small regions and create a diffusive-like structure with an effective migration length $\lambda_{mig} \gtrsim \lambda_{diff}$.

The α particles from ^{210}Po decays are selected event-by-event with a highly efficient α/β pulse shape discrimination neural network method based on a multi-layer perceptron (MLP)[50]. The resulting three-dimensional ^{210}Po activity distribution, named the low polonium field (LPoF), exhibits an effective migration profile with an almost stable minimum located above the detector equator (see 3D shape in Extended Data Fig. 5, and dark blue regions in Extended Data Fig. 6, top). The qualitative shape and approximate position of the LPoF is reproduced by fluid dynamical numerical simulations reported in ref. [30].

Assuming azimuthal symmetry around the detector z-axis, confirmed by 3D analysis, the ^{210}Po minimum activity is determined by fitting LPoF with a 2D paraboloidal function:

$$\frac{d^2R(^{210}\mathrm{Po})}{d(\rho^2)dz} = [R(^{210}\mathrm{Po}_{min})\epsilon_E\epsilon_{MLP} + R_\beta] \times \left(1 + \frac{\rho^2}{a^2} + \frac{(z-z_0)^2}{b^2}\right), \quad (4)$$

where $\rho^2 = x^2 + y^2$, a and b are the paraboloid axes, z_0 is the position of the minimum along the z axis, ϵ_E and ϵ_{MLP} are the efficiency of energy and MLP cuts used to select α particles from ^{210}Po decays, and R_β is the residual rate of β events after the selection of α particles. The fit is initially performed in data bins of 2 months, but compatible results are obtained using the bins of 1 month. Extended Data Fig. 6, top shows the result of the z_0 minimum position as a function of time. The minimum slowly moves along the z direction by less than 20 cm per month. In order to perform a better estimation of the ^{210}Po minimum, we sum up all the time bins after aligning the 3D distributions with respect to z_0. Possible intrinsic biases, due to the minimum determination in different time intervals, have been minimized by blindly aligning the data from each time bin according to the z_0 inferred from the previous time interval.

The distribution of ^{210}Po events after applying this procedure is shown in Extended Data Fig. 6, bottom, in which the LPoF structure is clearly visible. The final fit is then performed on 20 t of this aligned dataset containing about 5,000 ^{210}Po events. From this fit we extract the ^{210}Po minimum. This value might still have a small contribution from the vessel component (equation (2), that is, $R(^{210}\mathrm{Bi}) \leq R(^{210}\mathrm{Po}_{min})$). Therefore this method provides only an upper limit for the ^{210}Bi rate. A companion analysis was performed using a 3D paraboloidal function. The 2D and 3D fits were performed with a standard binned likelihood and a Bayesian approach using non-informative priors. In particular, the latter was implemented with MultiNest[51–53], a nested sampling algorithm.

In addition, because the shape of the LPoF might show more complexity along the z-axis than a simple paraboloidal shape, a Bayesian framework was also used to perform the fit with a cubic spline along the z axis. Splines are piecewise polynomials connected by knots. The number of knots defines the complexity of the curve. To prevent overfitting, a Bayesian factor analysis was used to decide on the most appropriate number of knots for the dataset. Although it was found that the splines were, in general, a better fit to the data (Bayes factor $>10^2$), the final result is compatible with the simpler model within statistical uncertainties. This result has been further cross-checked by fitting the ^{210}Po distribution along different angular directions with a family of analytical functions found as a solution of the Fick diffusion equation[54] for the migration of decaying ^{210}Po. Possible biases have been quantified by testing the fit model on simulated LPoF patterns based on numerical fluid dynamical simulations. They were found to be negligible for our purpose.

Spatial uniformity and time stability of ^{210}Bi

The ^{210}Bi independent constraint inferred from the LPoF can be extended over the whole fiducial volume if, and only if, the ^{210}Bi itself is uniform in space. Observation of the time stability of the ^{210}Bi rate, not strictly required if the time periods of the LPoF and main analyses

are the same, can additionally cross-check the overall robustness of the dataset.

We have evidence that at the beginning of Borexino Phase-II, after the purification campaign performed from 2010 to mid-2011, the ^{210}Bi was not uniform: the cleanest part of the scintillator was concentrated on the top, partially out of the fiducial volume. In fact, the purification was performed in loop, taking the scintillator out from the bottom, purifying it and re-inserting it from the top. For this reason, at the beginning of Phase-II the apparent ^{210}Bi rate was higher and slowly decreased over time as mixing was taking place, thanks to the strong pre-insulation convective currents. This decreasing trend stopped in early 2016, suggesting that the mixing had completed. Numerical fluid dynamical simulations, performed using the velocity field obtained from ^{210}Po movements during the pre-insulation time as input, confirm this hypothesis.

A more conservative approach, which uses heuristic arguments based on the effective migration of ions as measured from LPoF, suggests that ^{210}Bi at the beginning of Phase-III (mid-2016) must be uniform at least within a volume scale of about 20 m^3. This argument is also verified by means of fluid dynamics numerical simulations.

All the a priori arguments and qualitative studies described above are confirmed a posteriori by looking at the β event rate in optimized energy windows in which the ^{210}Bi signal-to-background ratio is maximal. The observed non-uniformity is then conservatively assigned only to ^{210}Bi, contributing about 15% to the overall rate in the selected energy window.

In order to test the spatial uniformity of the ^{210}Bi rate in the fiducial volume and to associate a systematic uncertainty to its possible non-uniformity, we split the spatial distribution into radial and angular components.

Extended Data Fig. 7 (top) shows the angular power spectrum of observed β events (black points). The dark pink and pink bands are the allowed 1σ and 2σ, regions respectively, obtained from 10^4 Monte Carlo simulations of uniformly distributed events. The analysis is performed with the HEALPix[55] software package, available, for example, for cosmic microwave background analysis.

Extended Data Fig. 7 (bottom) shows the linear fit to the r^3 distribution of the β events, expected to be flat for uniform spatial distribution, from which we determine the allowed residual non-uniformity along the radial direction.

All these studies show no evidence for a sizeable non-uniformity of the β-like event distribution inside the fiducial volume. In particular, the rate measured in the LPoF is fully consistent with that measured in the total fiducial volume. This evidence further supports a very small systematic uncertainty on the ^{210}Bi independent constraint. Combining in quadrature the uncertainties from the radial (0.52 cpd per 100 t) and angular (0.59 cpd per 100 t) components, we obtain a systematic error associated with the ^{210}Bi spatial uniformity of 0.78 cpd per 100 t.

Finally, we checked the stability of the ^{210}Bi rate over time by applying two methods on the observed rate of β events in the optimized energy windows: first, we studied the range of possible polynomial distortions; and second, we performed a Lomb–Scargle spectral decomposition (see ref. [56] and references therein). We found no evidence of any relevant time variation apart from the expected annual modulation due to solar neutrinos (^{7}Be-neutrinos contribute more than 60% to the β rate in the selected energy windows). Actually, the fact that we are capable of seeing the tiny 3.3% sinusoidal variation induced by the eccentricity of the Earth's orbit around the Sun is in itself further proof of the excellent stability of the ^{210}Bi rate over time. In particular, by studying the time dependence of the β-like events in the optimized window, the uncertainty in the ^{210}Bi rate change is 0.18 cpd per 100 t, which is indeed negligible as compared with the global error quoted in equation (3).

We note that, even after complete mixing, the true ^{210}Bi rate is not perfectly constant in time, as it must follow the decay rate of the parent ^{210}Pb (τ = 32.7 years). This effect is not detectable over the approximately 3-year time period of our analysis, but for substantially longer periods it could be used for better constraining the ^{210}Bi by fitting its long-lived temporal trend.

Details of the CNO analysis

The analysis presented in this work is based on the data collected from June 2016 to February 2020 (Borexino Phase-III) and is performed in a fiducial volume defined as $r < 2.8$ m and -1.8 m $< z < 2.2$ m (r and z being the reconstructed radial and vertical position, respectively). The total exposure of this dataset corresponds to 1,072 d × 71.3 t.

In Borexino, the energy of each event is given by the number of collected photoelectrons, whereas its position is determined by the photon arrival times at the PMTs. The energy and spatial resolution in Borexino has slowly deteriorated over time due to the steady loss of PMTs (the average number of active channels in Phase-III is 1,238) and is currently $\sigma_E/\sqrt{E} \approx 6\%$ and $\sigma_{x,y,z} \approx 11$ cm for 1 MeV events in the centre of the detector.

Events are selected by a sequence of cuts, which are specifically designed to veto muons and cosmogenic isotopes, to remove ^{214}Bi–^{214}Po fast coincidence events from the ^{238}U chain, electronic noise, and external background events. The fraction of neutrino events lost by this selection criteria is measured with calibration data to be of the order of 0.1% and is therefore negligible. More details on data selection can be found in ref. [20].

The main backgrounds surviving the cuts and affecting the CNO analysis are: ^{210}Bi and ^{210}Po in secular equilibrium with ^{210}Pb which, as discussed above, have a rate in Borexino Phase-III of $\leq 11.5 \pm 1.3$ cpd per 100 t; ^{210}Po^{V} from the vessel; ^{85}Kr (β, Q = 687 keV); ^{40}K (β and γ, Q = 1,460 keV); ^{11}C (β^+, Q = 960 keV; τ = 30 min), which is continuously produced by cosmic muons crossing the scintillator; and γ-rays emitted by ^{214}Bi, ^{208}Tl and ^{40}K from materials external to the scintillator (buffer liquid, PMTs, stainless steel sphere, etc.).

CNO neutrinos are disentangled from residual backgrounds using a multivariate analysis, which includes the energy and radial distributions of the events surviving the selection. Data are split into two complementary datasets: the threefold-coincidence (TFC)-subtracted spectrum, in which ^{11}C is selectively filtered out using the muon–neutron–positron threefold coincidence algorithm[19,57] and the TFC-tagged spectrum, enriched in ^{11}C. The TFC is a space and time coincidence vetoing the ^{11}C β^+ decay events, by tagging the spallation muon and the neutron capture from the reactions: $\mu + {}^{12}\mathrm{C} \rightarrow {}^{11}\mathrm{C} + n$ and $n + p \rightarrow \mathrm{d} + \gamma$. The reference shapes—that is, the probability density functions (PDFs) for signal and backgrounds used in the fit—are obtained through a complete Geant4-based Monte Carlo code[31], which simulates all physics processes occurring in the scintillator, including energy deposition, photon emission, propagation, and detection, generation and processing of the electronic signal. The simulation takes into account the evolution in time of the detector response and produces data that are reconstructed and selected following the same pipeline of real data. The relevant input parameters of the simulation—mainly related to the optical properties of the scintillator and of the surrounding materials—have been initially obtained through small-scale laboratory tests and subsequently fine-tuned on calibration data, reaching an agreement at the sub-per-cent level[35]. Data are then fitted as the sum of signal and background PDFs: the weights of this sum (the energy integral of the rates with zero threshold of each component in Borexino) are the only free parameters of the fit. The details of the multivariate fit tool, used also to perform other solar neutrino analysis in Borexino, are described thoroughly in refs. [3,20]. Contrary to the previous comprehensive *pp* chain analysis, the fit is performed between 320 and 2,640 keV, thus excluding the contribution of ^{14}C decays and its pile-up. This choice is motivated by the loss of energy and position resolutions due to the decreased number of active channels in Phase-III, which affects mainly the low-energy region.

In addition to the energy shape, other information is exploited to help the fit to disentangle the signal from background: the ^{11}C β^+ events are

tagged by TFC, and contributions from the external backgrounds (^{208}Tl, ^{214}Bi and ^{40}K) are further constrained due to their radial distribution.

In order to enhance the sensitivity to CNO neutrinos, the *pep* neutrino rate is constrained to the value 2.74 ± 0.04 cpd per 100 t derived from a global fit[25,26] to solar neutrino data and imposing the *pp*/*pep* ratio and the solar luminosity constraint, considering the Mikheyev–Smirnov–Wolfenstein matter effect on the neutrino propagation, as well as the errors on the neutrino oscillation parameters. As discussed in the main text, the spectral fit has little capability to disentangle events due to CNO neutrino interactions and ^{210}Bi decay. Therefore, we use the results of the independent analysis on the ^{210}Po distribution in the LPoF to set an upper limit to the ^{210}Bi rate of 11.5 ± 1.3 cpd per 100 t.

The results of the simultaneous multivariate fit are given in Extended Data Fig. 8, showing the TFC-subtracted and TFC-tagged energy spectra, and in Extended Data Fig. 9, demonstrating the fit of the radial distribution. The fit is performed in the energy estimator N_h (defined as the sum of all photons triggering a PMT, normalized to 2,000 active PMTs) and the results are reported also in keV. The *P* value of the fit is 0.3, demonstrating fair agreement between data and the underlying fit model. A non-zero CNO neutrino rate is clearly better suited to the fit, as shown in the log-likelihood profile of Fig. 4 (dashed black curve).

Many sources of possible systematic errors have been considered. The systematic error associated with the fit procedure was studied by performing 2,500 fits with slightly altered conditions (different fit ranges and binning), and was found to be negligible with respect to the statistical uncertainty.

Because the multivariate analysis relies critically on the simulated PDFs of signal and backgrounds, any mismatch between the realistic and simulated energy shapes can alter the result of the fit and bias the significance on the CNO neutrinos. In order to study the effect of these possible mismatches, we simulated more than a million pseudo-datasets with the same exposure as Phase-III, injecting deformations in the signal and background shapes, following ref. [58]. Each dataset is then fitted with the standard non-deformed PDFs. The study was performed injecting different values of CNO, including the one obtained by our best fit. We studied the effect of the following sources of deformations:

(1) Energy response function: inaccuracies in the energy scale (at the level of ~0.23%) and in the description of non-uniformity and nonlinearity of the response (at the level of ~0.28% and ~0.4%, respectively). The size of the applied deformations has been chosen in the range allowed by calibration data and by data from specific internal backgrounds (^{11}C and ^{210}Po) taken as reference 'standard candles'.

(2) Deformations of the ^{11}C spectral shape induced by cuts to remove noise events, not fully taken into account by the Monte Carlo PDFs (at the level of 2.3%).

(3) Spectral shape of ^{210}Bi: we studied the systematic error associated with the shape of the forbidden β-decay of ^{210}Bi simulating data with alternative spectra (found in refs. [33,34]) with respect to the default spectrum[32]. Differences in the shapes may be as large as 18%.

From this Monte Carlo study we evaluate the CNO systematic error due to a mismatch between real and simulated PDFs to be $^{+0.6}_{-0.5}$ cpd per 100 t. This uncertainty is deduced by comparing the CNO output distributions from toy Monte Carlo PDFs with and without injecting systematic distortions as described above.

In order to evaluate the significance (space) of our result in rejecting the no-CNO hypothesis, we performed a frequentist hypothesis test using a profile likelihood test, with statistics *q* defined (following ref. [38]) as:

$$q = -2\log\frac{\mathcal{L}(\mathrm{CNO}=0)}{\mathcal{L}(\mathrm{CNO})}, \quad (5)$$

where $\mathcal{L}(\mathrm{CNO}=0)$ and $\mathcal{L}(\mathrm{CNO})$ is the maximum likelihood obtained by keeping the CNO rate fixed to zero or free, respectively. Extended Data Fig. 10 shows the *q* distribution obtained from 13.8 million pseudo-datasets simulated with deformed PDFs (see above) and no-CNO injected (q_0, grey curve). In the same plot, the theoretical q_0 distribution in the case of no PDF deformation is shown (blue curve). The result of data obtained from the fit is the black line ($q_{\mathrm{data}} = 30.05$).

The plot in Extended Data Fig. 10 enables us to reject the CNO = 0 hypothesis with a significance better than 5.0σ at 99.0% confidence level[59]. This construction is consistent with the significance evaluation of 5.1σ, reported in the main text, by means of the quantiles of the profile likelihood folded with the systematic uncertainty.

In Extended Data Fig. 10, we also provide as reference the *q* distribution (red) obtained with 1 million pseudo-datasets, including systematic deformations and injected CNO rate equal to 7.2 cpd per 100 t—that is, our best fit value.

A cross-check of the main analysis has been performed with an almost independent method—counting analysis—in which we simply count events in an optimized energy window (region of interest, ROI) and subtract the contributions due to known backgrounds in order to reveal the CNO signal. This method is simpler, albeit less powerful, with respect to the multivariate fit and is less prone to possible correlations between different species. However, whereas the multivariate analysis implicitly checks the validity of the background model by the goodness of the fit, the counting analysis relies completely on the assumption that there are no unknown backgrounds that contribute to the ROI.

The counting analysis is based on a different energy estimator than the multivariate analysis ($\mathcal{N}_{\mathrm{pe}}$, the total charge of all hits, normalized to 2,000 active channels) and relies on a different response function (analytically derived, instead of Monte Carlo-based) to determine the percentage of events for each of the signal and background species that falls inside the ROI. The chosen ROI, 780–885 keV, is obtained optimizing the CNO signal-to-background ratio. An advantage of this method is that, in the ROI, some of the backgrounds that affect the multivariate analysis (such as ^{85}Kr and ^{210}Po) are not present or contribute less than 2% (for example, external backgrounds). The count rate is dominated by CNO, *pep* and ^{210}Bi (80%), with smaller contributions from ^{7}Be neutrinos and residual ^{11}C (18%). The rate of *pep* neutrinos and ^{210}Bi are constrained to the same values used in the multivariate fit. Note that whereas in the spectral fit the ^{210}Bi rate is left free to vary between 0 up to 11.5 ± 1.3 cpd per 100 t (the upper limit determined in the LPoF analysis), the counting analysis conservatively constrains it to the maximum value with a Gaussian error of 1.3 cpd per 100 t. The ^{7}Be neutrino rate is sampled uniformly between the low-metallicity (43.7 ± 2.5 cpd per 100 t) and the high-metallicity (47.9 ± 2.8 cpd per 100 t) values predicted by the Standard Solar Model[17] with 1σ error, whereas the ^{11}C rate is obtained from the average Borexino Phase-II results with an additional conservative error of 10% derived from uncertainties on the energy scale (quenching of the 1 MeV annihilation γ-rays). The CNO rate is obtained by subtracting all background contributions defined above and by propagating the uncertainties by randomly sampling their rates from Gaussian distributions with proper widths. Note that the uncertainty related to the energy response (which affects the percentage of the spectrum of each component falling in the ROI) also contributes to the total error associated with the count rate of each species.

The CNO rate obtained with this method is demonstrated by the red histogram in Fig. 4. The mean value and width of the distribution are 5.6 ± 1.6 cpd per 100 t, confirming the presence of CNO at the 3.5σ level.

The counting analysis shows that the core of the sensitivity to CNO neutrinos in Borexino mainly comes, as expected, from a narrow energy region in which the contributions from CNO, *pep* and ^{210}Bi are dominant over the residual backgrounds, as discussed in ref. [24]. Conversely, the multivariate fit effectively exploits additional information contained in the data with a substantial enhancement of the significance of the CNO solar neutrino.

Data availability

The datasets generated during the current study are freely available from the repository https://bxopen.lngs.infn.it/. Additional information is available from the Borexino Collaboration spokesperson (spokesperson-borex@lngs.infn.it) upon reasonable request.

42. Birks, J. B. *The Theory and Practice of Scintillation Counting* (Pergamon, 1964).
43. Benziger, J. et al. The scintillator purification system for the Borexino solar neutrino detector. *Nucl. Instrum. Methods Phys. Res. A* **587**, 277–291 (2008).
44. Alimonti, G. et al. The liquid handling systems for the Borexino solar neutrino detector. *Nucl. Instrum. Methods Phys. Res. A* **609**, 58–78 (2009).
45. Bellini, G. et al. Cosmic-muon flux and annual modulation in Borexino at 3800 m water-equivalent depth. *J. Cosmol. Astropart. Phys.* **2012**, 015 (2012).
46. Bellini, G. et al. Cosmogenic backgrounds in Borexino at 3800 m water-equivalent depth. *J. Cosmol. Astropart. Phys.* **2013**, 049 (2013).
47. Bellini, G. et al. Muon and cosmogenic neutron detection in Borexino. *J. Instrum.* **6**, P05005 (2011).
48. Cruickshank Miller, C. The Stokes–Einstein law for diffusion in solution. *Proc. R. Soc. Lond. A* **106**, 724–729 (1924).
49. Wójcik, M., Wlazlo, W., Zuzel, G. & Heusser, G. Radon diffusion through polymer membranes used in the solar neutrino experiment Borexino. *Nucl. Instrum. Methods Phys. Res. A* **449**, 158–171 (2000).
50. Hoecker, A., Speckmayer, P., Stelzer, J., Therhaag, J., von Toerne, H. & Voss, E. TMVA - toolkit for multivariate data analysis. Preprint at https://arxiv.org/abs/physics/0703039 (2007).
51. Feroz, F., Hobson, M. P., Cameron, E. & Pettitt, A. N. Importance nested sampling and the MultiNest algorithm. *Open J. Astrophys.* **2**, 10 (2019).
52. Feroz, F., Hobson, M. P. & Bridges, M. MultiNest: an efficient and robust Bayesian inference tool for cosmology and particle physics. *Mon. Not. R. Astron. Soc.* **398**, 1601–1614 (2009).
53. Feroz, F. & Hobson, M. P. Multimodal nested sampling: an efficient and robust alternative to Markov Chain Monte Carlo methods for astronomical data analyses. *Mon. Not. R. Astron. Soc.* **384**, 449–463 (2008).
54. Fick, A. Ueber Diffusion. *Ann. Phys.* **170**, 59–86 (1855).
55. Gorski, K. M., Wandelt, B. D., Hansen, F. K., Hivon, E. & Banday, A. J. The HEALPix Primer. Preprint at https://arxiv.org/abs/astro-ph/9905275 (1999).
56. Agostini, M. et al. Seasonal modulation of the ^{7}Be solar neutrino rate in Borexino. *Astropart. Phys.* **92**, 21–29 (2017).
57. Bellini, G. et al. First evidence of *pep* solar neutrinos by direct detection in Borexino. *Phys. Rev. Lett.* **108**, 051302 (2012).
58. Cousins, R. D. & Highland, V. L. Incorporating systematic uncertainties into an upper limit. *Nucl. Instrum. Methods Phys. Res. A* **320**, 331–335 (1992).
59. Brown, L. D., Cai, T. T. & Das Gupta, A. Interval estimation for a binomial proportion. *Stat. Sci.* **16**, 101–133 (2001).

Acknowledgements We acknowledge the hospitality and support of the Laboratori Nazionali del Gran Sasso (Italy). The Borexino program is made possible by funding from Istituto Nazionale di Fisica Nucleare (INFN) (Italy), National Science Foundation (NSF) (USA), Deutsche Forschungsgemeinschaft (DFG) and Helmholtz-Gemeinschaft (HGF) (Germany), Russian Foundation for Basic Research (RFBR) (grant numbers 16-29-13014ofi-m, 17-02-00305A and 19-02-00097A), Russian Science Foundation (RSF) (grant number 17-12-01009) and Ministry of Science and Higher Education of the Russian Federation (contract number 075-15-2020-778) (Russia), and Narodowe Centrum Nauki (NCN) (grant number UMO 2017/26/M/ST2/00915) (Poland). We acknowledge the computing services of Bologna INFN-CNAF data centre and U-Lite Computing Center and Network Service at LNGS (Italy), and the computing time granted through JARA on the supercomputer JURECA at Forschungszentrum Jülich (Germany). This research was supported in part by PLGrid Infrastructure (Poland).

Author contributions The Borexino detector was designed, constructed and commissioned by the Borexino Collaboration over the span of more than 30 years. The Borexino Collaboration sets the science goals. Scintillator purification and handling, material radiopurity assay, source calibration campaigns, photomultiplier tube and electronics operations, signal processing and data acquisition, Monte Carlo simulations of the detector, and data analyses were performed by Borexino members, who also discussed and approved the scientific results. This Article was prepared by a subgroup of authors that was appointed by the Collaboration and was subjected to an internal collaboration-wide review process. All authors reviewed and approved the final version of the manuscript.

Competing interests The authors declare no competing interests.

Additional information

Supplementary information is available for this paper at https://doi.org/10.1038/s41586-020-2934-0.

Correspondence and requests for materials should be addressed to G.R.

Peer review information *Nature* thanks Marc Pinsonneault, Gabriel Orebi Gann and David Wark for their contribution to the peer review of this work. Peer reviewer reports are available.

Reprints and permissions information is available at http://www.nature.com/reprints.

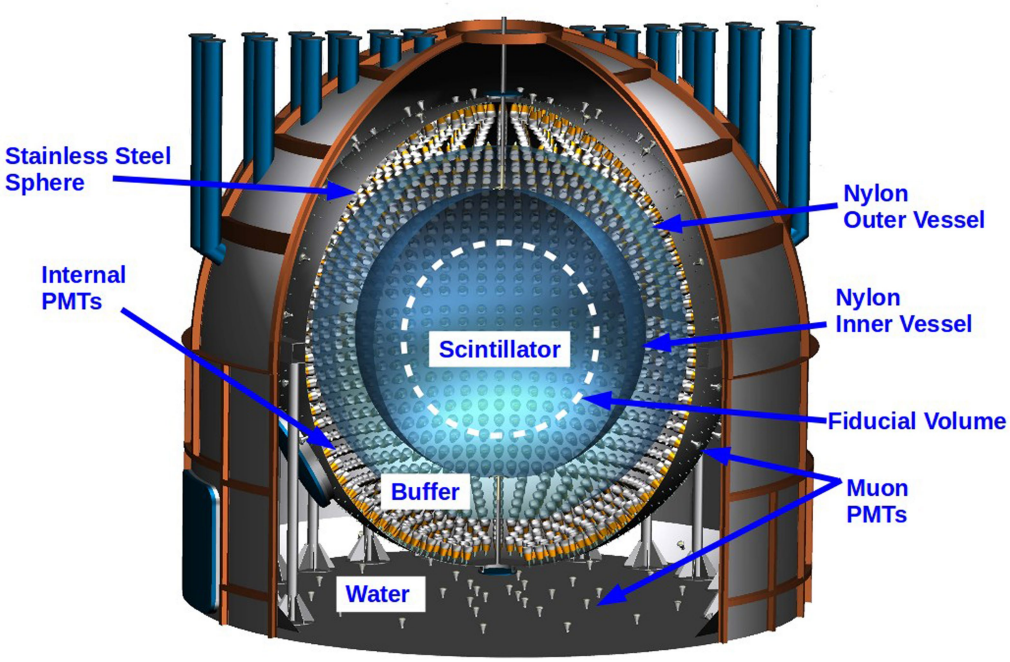

Extended Data Fig. 1 | The Borexino detector. Schematic view of the structure of the Borexino apparatus. From inside to outside: the liquid scintillator, the buffer liquid, the stainless steel sphere with the photomultipliers, and the water tank.

Extended Data Fig. 2 | The Borexino detector after the thermal stabilization. The Borexino water tank after completion of the thermal insulation and deployment of the active temperature control system.

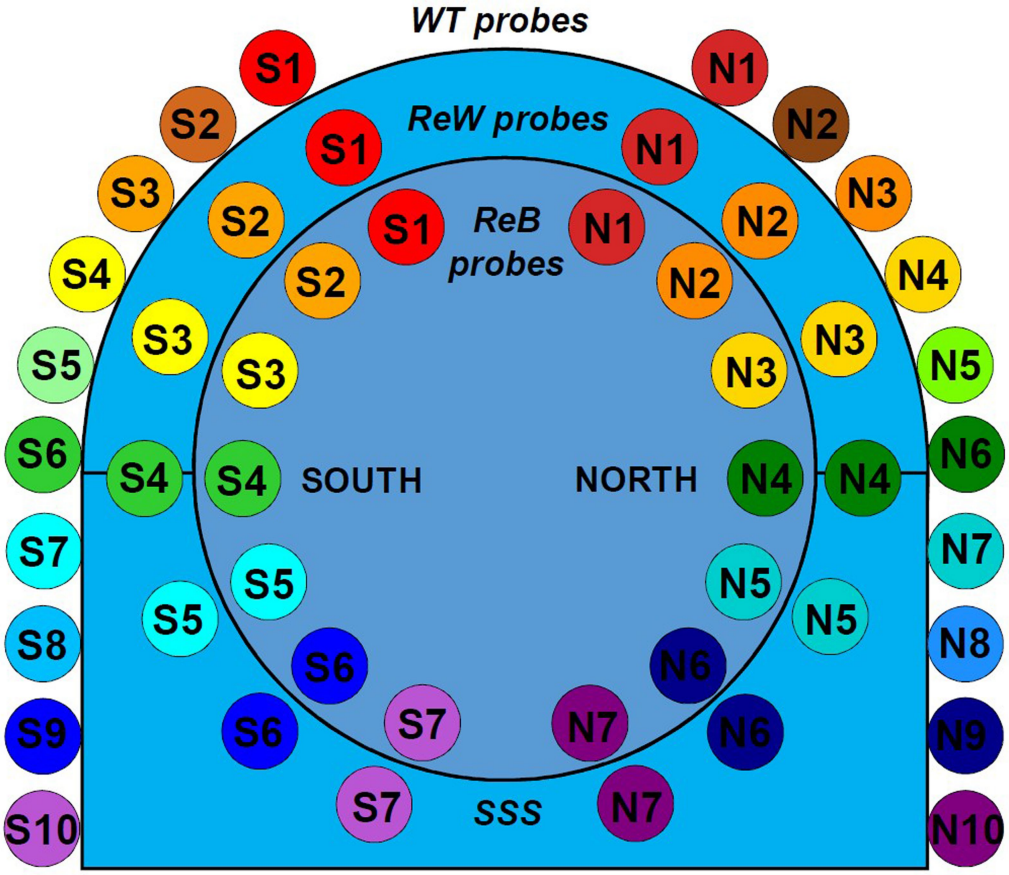

Extended Data Fig. 3 | Temperature probes of the Borexino detector. Distribution of temperature probes around and inside the Borexino detector. For simplicity, the probes on the water tank (WT) dome and in the pit below the detector are not shown.

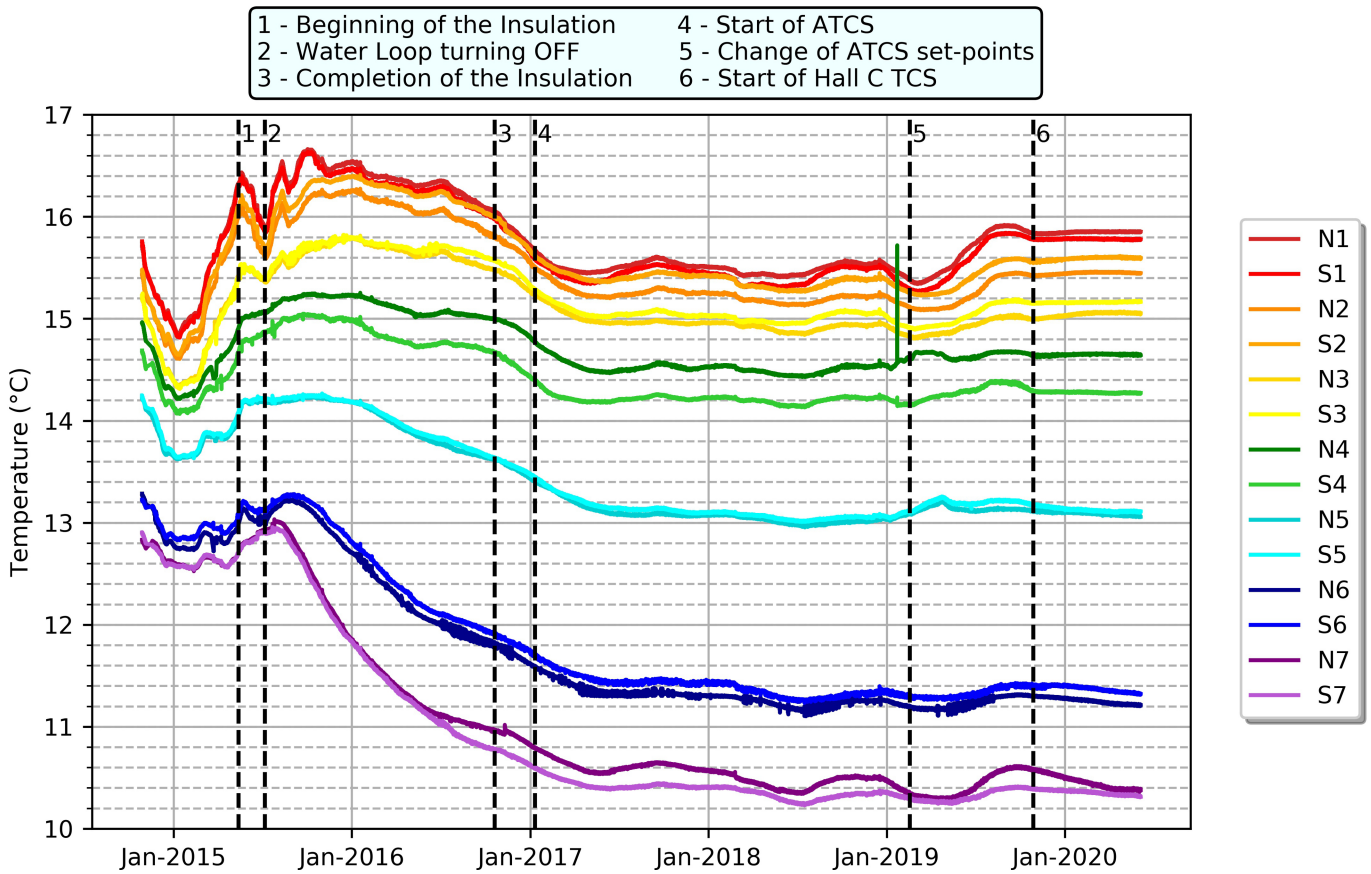

Extended Data Fig. 4 | Temperature evolution over time in the Borexino detector. Graph depicting the temperature as a function of time in different volumes of the Borexino detector. The vertical dashed lines show the beginning of the thermal insulation installation (1), the turning off of the water loop inside the water tank (2), the completing of the thermal insulation installation (3), the activation of the temperature control system on the dome of the water tank (4), the set-point change (5) and the activation of the air control system in experimental hall C (6).

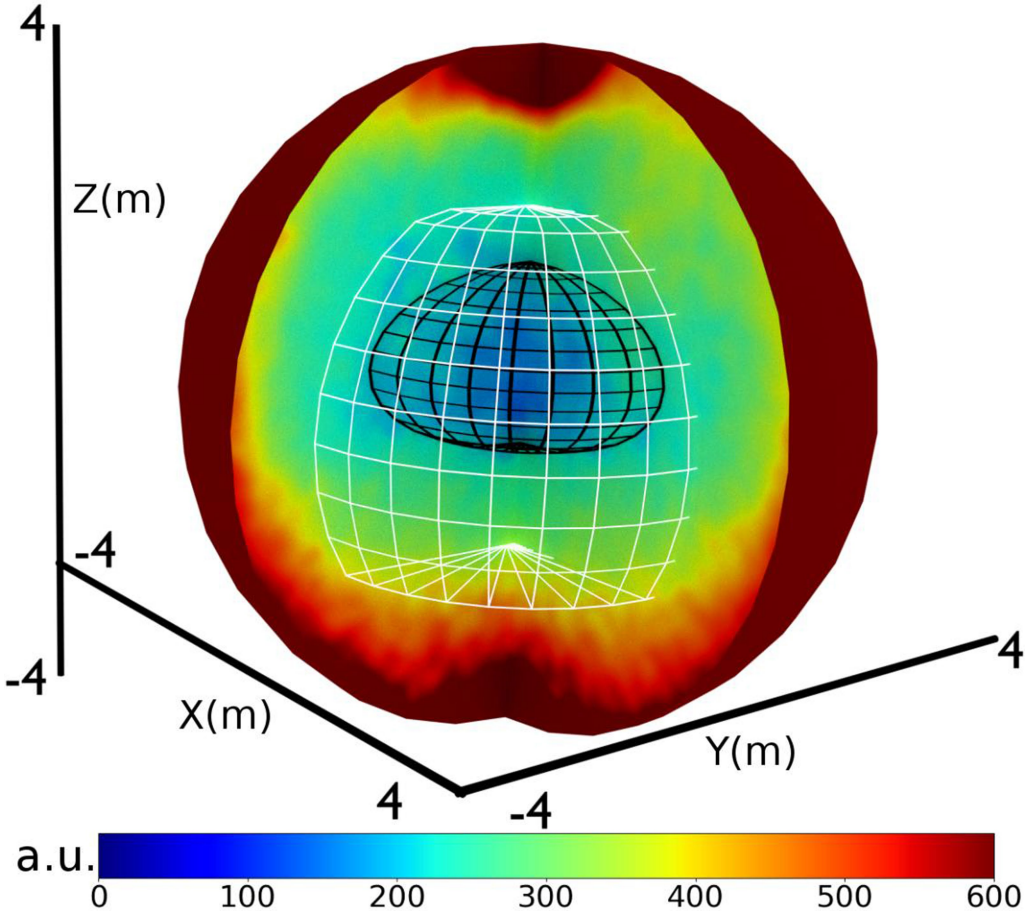

Extended Data Fig. 5 | The low polonium field in the Borexino scintillator. Three-dimensional view of the ^{210}Po activity inside the entire nylon vessel (see colour code). The innermost blue region contains the LPoF (black grid). The white grid is the software-defined fiducial volume. a.u., arbitrary units.

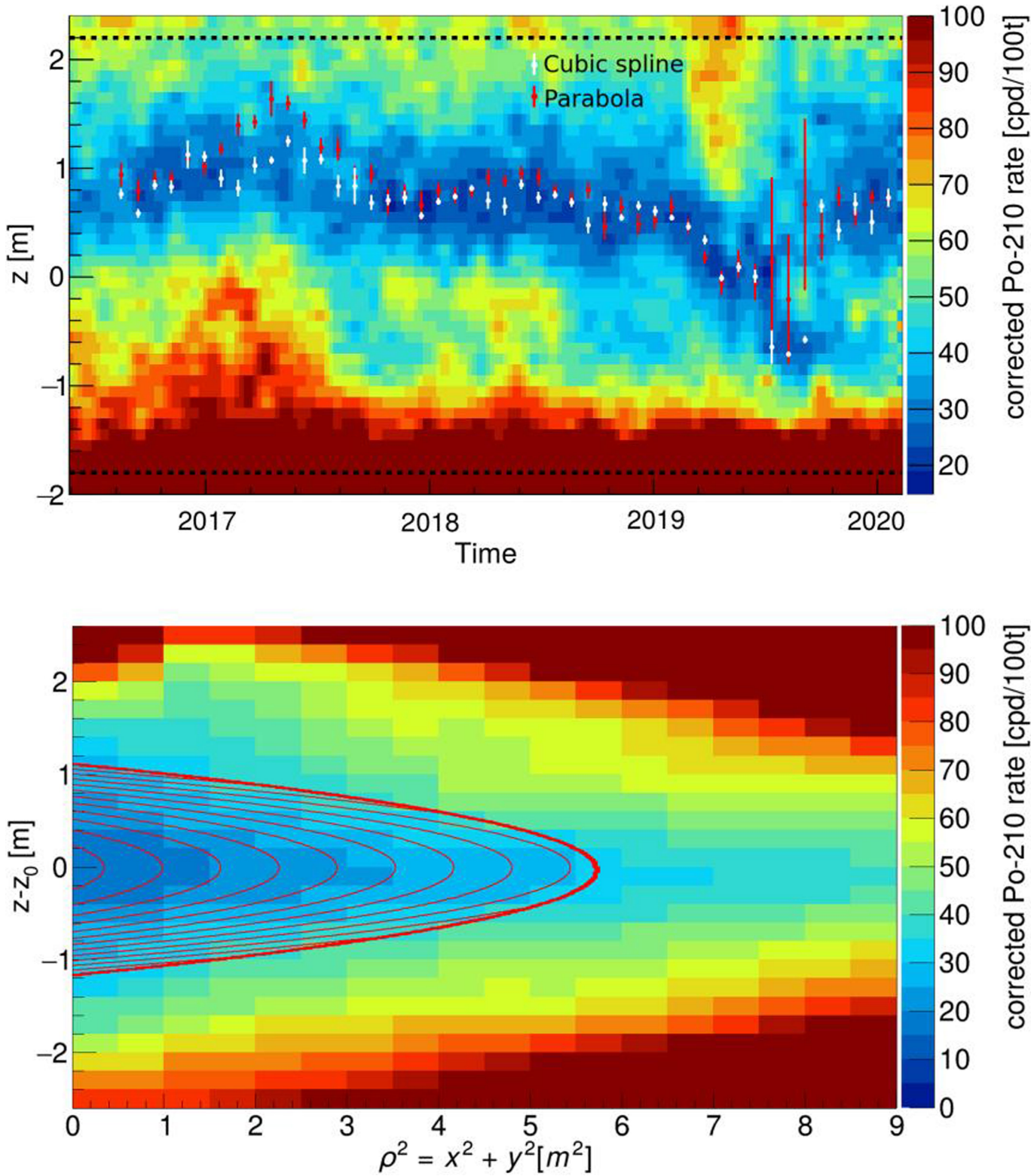

Extended Data Fig. 6 | Analysis of the low polonium field. Top, the rate of ^{210}Po in cylinders of 3-m radius and 10-cm height located along the z axis from −2 m to 2 m, as a function of time with 1-month binning. The dashed lines indicate the z coordinate of the fiducial volume. The markers show the positions of the centre of the LPoF obtained with two fit methods: paraboloid (red) and spline (white). Both fit methods follow the dark-blue minimum of the ^{210}Po activity well. The structure visible in mid-2019 is due to a local instability produced by a tuning of the active temperature control system. This transient has no effect on the final result. Bottom, distribution of ^{210}Po events after the blind alignment of data using the z_0 from the paraboloidal fit (red markers in the top graph). The red solid lines indicate the paraboloidal fit within 20 t with equation (4).

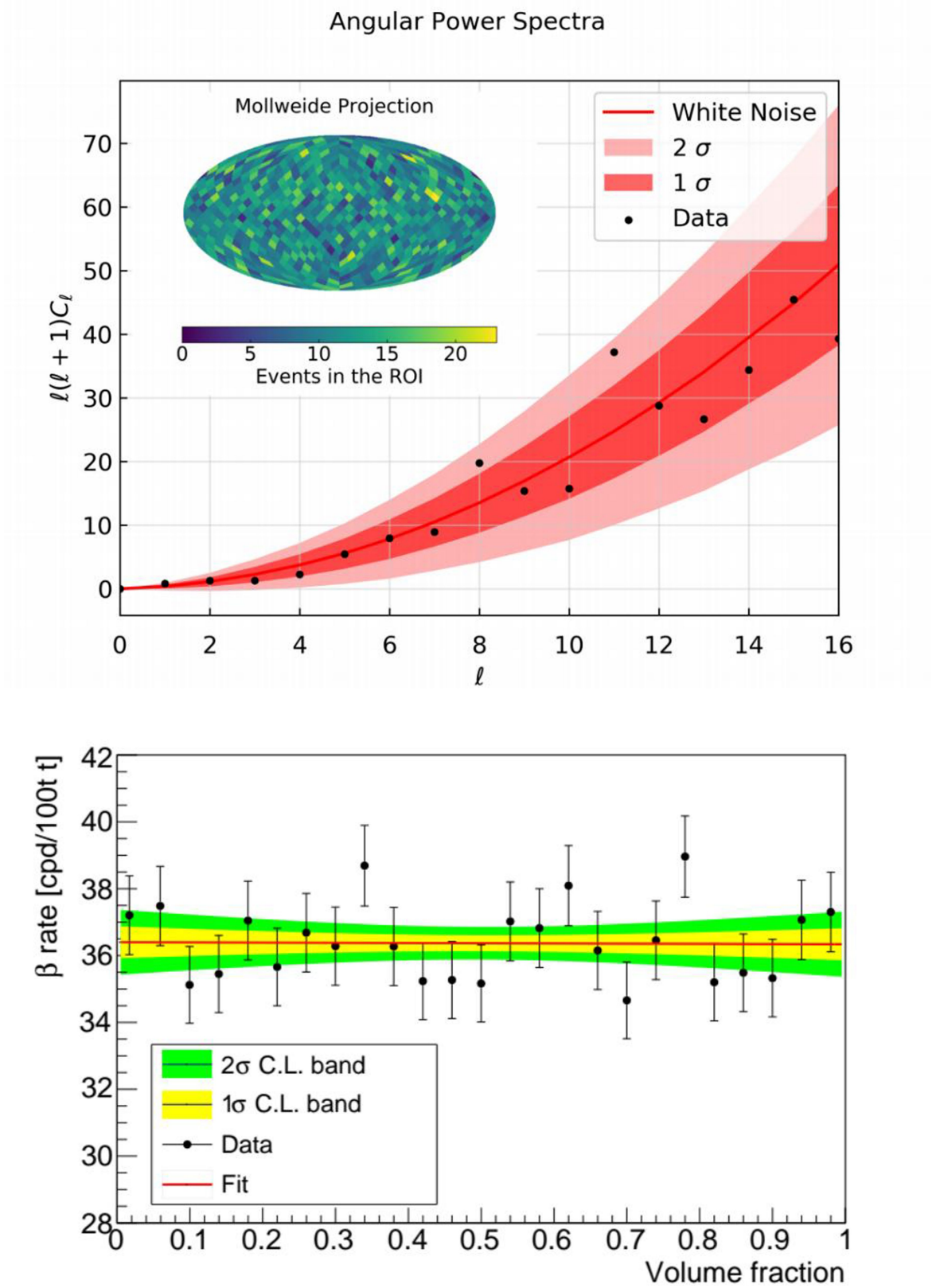

Extended Data Fig. 7 | Angular and radial uniformity of the β events in the optimized energy window. Top, angular power spectrum as a function of the multipole moment l of observed β events (black points) compared with 10^4 uniformly distributed events from Monte Carlo simulations at 1σ (dark pink) and 2σ (pink) confidence levels (C.L.). Data are compatible with a uniform distribution within the uncertainty of 0.59 cpd per 100 t. Inset, angular distribution of the β events. Bottom, normalized radial distribution of β events r/r_0 (black points), where $r_0 = 2.5$ m is the radius of the sphere surrounding the analysis fiducial volume. The linear fit of the data (red solid line) is shown along with the 1σ (yellow) and 2σ (green) confidence level bands. The data are compatible with a uniform distribution within 0.52 cpd per 100 t.

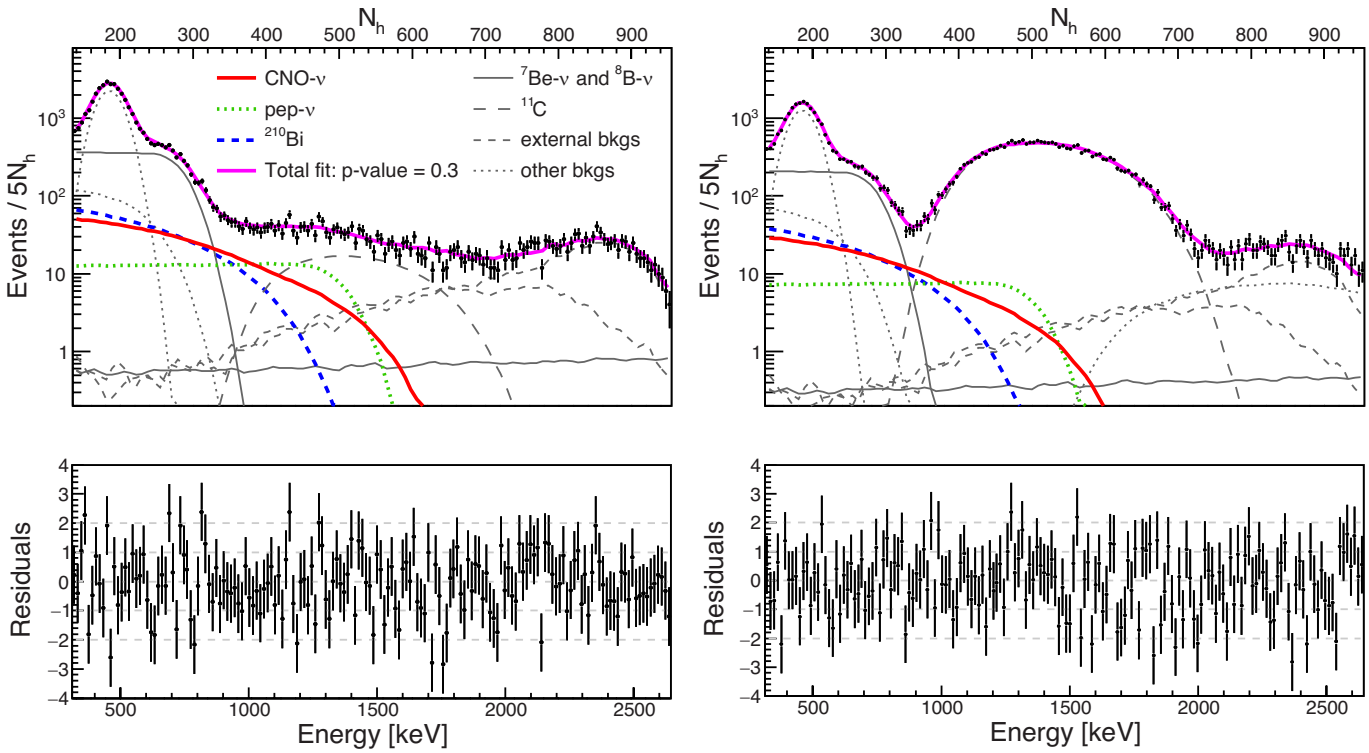

Extended Data Fig. 8 | Energy distributions from a multivariate fit of the Borexino data. Full multivariate fit results for the TFC-subtracted (left) and the TFC-tagged (right) energy spectra with corresponding residuals. In both graphs the magenta lines represent the resulting fit function, the red line is the CNO neutrino electron recoil spectrum, the green dotted line is the *pep* neutrino electron recoil spectrum, the dashed blue line is the ^{210}Bi β spectrum, and in grey we report the remaining background (bkgs) contributions.

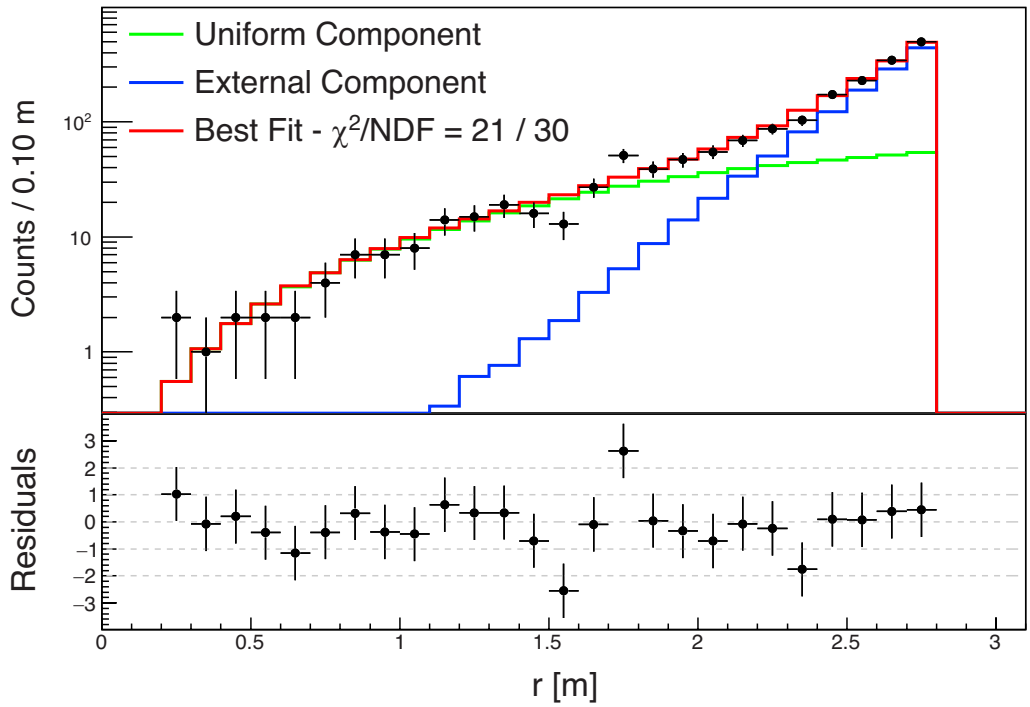

Extended Data Fig. 9 | Radial distribution from a multivariate fit of the Borexino data. Radial distribution of events in the multivariate fit. The red line is the resulting fit, the green line represents the internal uniform contribution and the blue line shows the non-uniform contribution from the external background. NDF, the number of degrees of freedom in the fit.

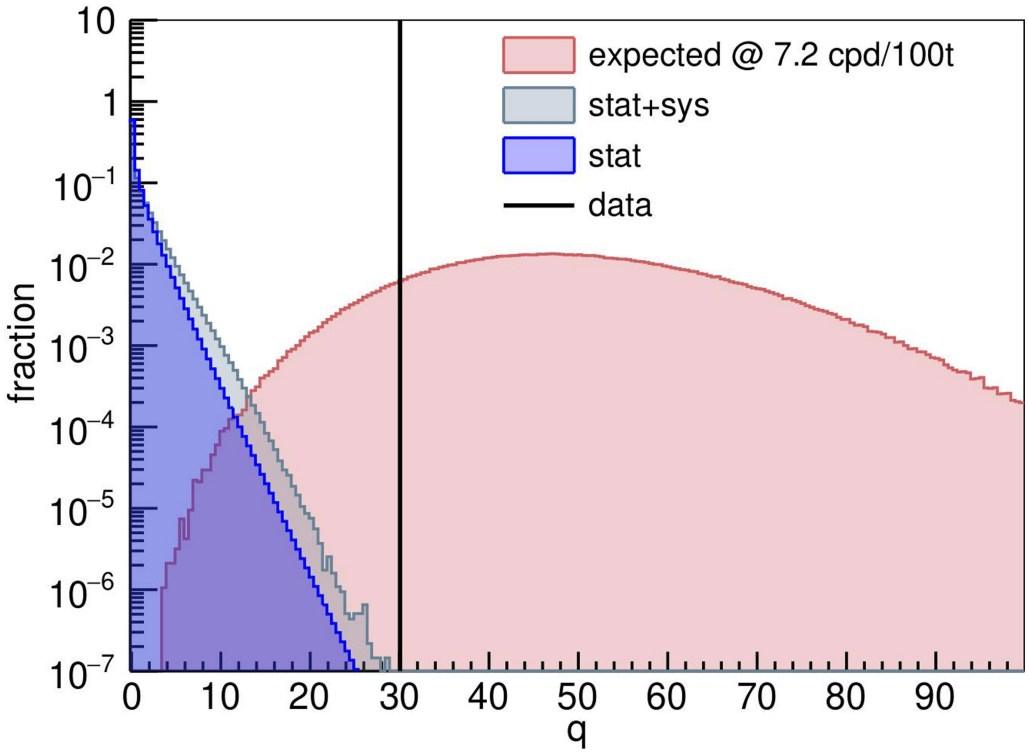

Extended Data Fig. 10 | Frequentist hypothesis test for the CNO observation. Distribution of the test statistics q (equation (5) from Monte Carlo pseudo-datasets). The grey distribution q_0 is obtained with no CNO simulated data and includes the systematic uncertainty. The black vertical line represents $q_{data} = 30.05$. The corresponding P value of q_0 with respect to q_{data} gives the significance of the CNO discovery (>5.0σ at 99% confidence level). For comparison, in blue is the q_0 without the systematics. The red histogram represents the expected test statistics distribution for an injected CNO rate equal to 7.2 cpd per 100 t—that is, our best fit value.